UNIVERSITY OF CANTERBURY

Department of Physics and Astronomy

CHRISTCHURCH NEW ZEALAND

Crystal Field Matrix Reduction and Polarisation Interference Calculations

Michael James Lee

MASTERS THESIS

February 1999

Abstract

The theory of one-electron crystal field parametrisation for optical spectra of rare-earth doped crystalline lattices dates back over forty years. The effect of the crystal host material is to split the free-ion degeneracy of the rare-earth multiplets. Some of these multiplets have structure which defies explanation in terms of crystal field theory and new developments have emerged within the last five years to address the problem. One of these methods takes the set of crystal field operators and appends two-electron correlation operators. Another adjusts the crystal field operators to include excited state configuration effects. A direct comparison of fitted parameters is meaningless, the corresponding operators being defined on different spaces. Here the techniques of matrix reduction, as developed in effective operator theory, are applied to larger configuration Hamiltonians to model their effects in correlation space. Correlation operators are then fitted to the reduced configuration matrices to establish a connection between the two approaches.

Transition intensity parametrisation has a similar lengthy history and formulation. Geometric effects first brought to light fifteen years ago suggest the possibility of polarisation dependent interference between the transition moments of different Cartesian axes. This would manifest itself in the directional dependence of fluorescence intensity for low symmetry crystal hosted rare-earth centres. To date there have been no experimental tests of these predictions and here a case is made for certain transitions of hydrogenated praseodymium doped fluorite. There are certain practical difficulties which must be overcome and these are also addressed.

Acknowledgements

This thesis was undertaken with the supervision of Mike Reid and Phil Butler, and funded by Marsden grant number UOC704.

Thanks are extended to Michele Faucher for provision of the configuration interaction Hamiltonians, to Keith Murdoch for useful discussions on polarisation behaviour, to Noel Doughty and Mike Reid for help with ¡#*@%⋆! LaTeX, to Luke McAven for RACAH assistance, and to Karl Roozen for pointers on FREEHAND.

Also to Jeff Raskin and the Macintosh design team, Jason Jones and fellow runners (wilful and non-wilful), and of course to small furry animals.

Contents

Figures

Tables

Chapter 1

Crystal Field Calculations

First things first — but not necessarily in that order. – *Doctor Who*

1.1 Introduction

Over the last forty years there have been extensive experimental studies of rare-earth doped crystals and their optical spectra [10, 17, 20, 31] which are dominated by the unfilled $4f^N$ configuration. Contemporary theoretical parametrisation of atomic "free-ion" interactions and effects from the crystal (or "crystal field") have become well established [5, 11, 13, 20, 22, 30, 32]. Once the site symmetry of the rare-earth ion centre is known, operators describing specific physical interactions may be generated as matrices by the Wigner-Eckart theorem and fitted to experimentally determined energy levels by the method of least squares. This produces a Hamiltonian for the system as a sum of operators multiplied by (fitted) parameters. In its original formulation this theory consisted of various operators describing specific Coulombic free-ion and spin-orbit interactions plus a Crystal-Field (CF) Hamiltonian, the conventional one-electron form of which is expressed as a sum of tensor operators $\mathrm{C}_q^{(k)}$ scaled by parameters B_q^k [13]. The operators are defined very simply as renormalised spherical harmonics Y_q^k, identifying k as an orbital angular momentum quantum number and q with its z axis projection.

$$\mathrm{H}_{CF} = \sum_{kq} B_q^k \mathrm{C}_q^{(k)} \tag{1.1}$$

$$\mathrm{C}_q^{(k)} \equiv \sqrt{\frac{4\pi}{2k+1}} \mathrm{Y}_q^k \tag{1.2}$$

Whereas the electrostatic and spin-orbit terms effect large scale degeneracy splitting between whole multiplets, crystal field operators provide smaller adjustments to individual energy levels within each multiplet. This form traditionally acts only within the $4f^N$ configuration and does not take two-electron (correlation) or excited-state (configuration) effects into account. Technically both two-electron and excited-state interactions are forms of correlation effect, but here the word correlation shall

be used exclusively to denote two-electron $4f^N$ interactions and configuration shall refer only to excited-state single-electron interactions. That analyses using equation (1.1) give good fits to most of the observed crystal field splitting in crystal perturbed lanthanide spectra can be taken as evidence that two-electron CF effects are relatively small, but a few anomalous multiplets have continually defied explanation [5, 22, 30], acquiring a certain degree of notoriety [12].

In response to these observed discrepancies, some comparatively recent modifications have been made to the CF formulation [33] which expand upon the above parametrisation. There are two main approaches to this, one includes correlation effects, the other configuration interactions. Correlation methods [5] include both free-ion and crystal field operators in unmodified form and append Correlation Crystal Field (CCF) operators to the total formulation. The CCF Hamiltonian is a sum of parameters G^k_{iq} multiplying spin-independent two-electron operators $\mathrm{g}^{(k)}_{iq}$. These have some of the same transformation properties as the $\mathrm{C}^{(k)}_q$'s operators and the angular momentum quantum numbers k and q turn out to be convenient labels once again.

$$\mathrm{H}_{CCF} = \sum_{kqi} G^k_{iq} \mathrm{g}^{(k)}_{iq} \tag{1.3}$$

The other approach [11] is to perform configuration-mixing crystal field calculations in which the basis set is extended by appending single-excited-electron states (*e.g.* $4f^{N-1}6p$) to the $4f^N$ states. Whereas CCF calculations produce a total Hamiltonian including free-ion parameters plus H_{CF} plus H_{CCF}, the configuration interaction method extends the CF equation (1.1) by including crystal field interactions not only within the $4f^N$ configuration (ff), but also coupling to the excited $4f^{N-1}6p$ configuration (fp) by single-electron operator crystal field and Coulomb interactions. There are no immediate new operators (although it often proves computationally convenient to split the spherical harmonics into separate terms for excited and unexcited states), but the basis set of states over which they are defined has been increased. For this reason, the technique is referred to as an Extended Basis Set (EBS) configuration interaction calculation.

The CCF Hamiltonian is defined on a $4f^N$ basis and is a $4f^N$ Hamiltonian, straightforwardly enough. However, the basis for the EBS Hamiltonian is formed as a direct sum of the $4f^N$ and $4f^{N-1}6p$ bases *viz.* $4f^N \oplus 4f^{N-1}6p$, but these states are not crystal perturbed eigenstates; there are interactions between them for a crystal perturbed ion. This translates as cross-terms between the $4f^N$ and $4f^{N-1}6p$ basis functions of the EBS Hamiltonian, which cannot, therefore, be written as a direct

sum of $4f^N$ and $4f^{N-1}6p$ sub-Hamiltonians itself. The EBS shall be referred to a $4f^N + 4f^{N-1}6p$ Hamiltonian acting within a convoluted $4f^N + 4f^{N-1}6p$ space, but defined against a $4f^N \oplus 4f^{N-1}6p$ basis.

Despite their differences both approaches give similar fits to experimental data, but because the two methods use operators from different spaces a direct comparison of their parameter sets is meaningless. Both methods may have a parameter pertaining to some particular physical interaction, B_4^6 say, but the matrix representations of the corresponding operator will have different dimensions and physical interpretations for each method.

By reducing the EBS Hamiltonian from $4f^N + 4f^{N-1}6p$ space down to $4f^N$ space with a transformation that retains all $4f^N \rightleftharpoons 4f^{N-1}6p$ configuration interaction effects upon the $4f^N$ states, it becomes possible to fit CCF operators to the $4f^N$ component of the EBS Hamiltonian. It will be shown that inclusion of configuration interaction effects is broadly equivalent to using CCF operators.

Three specific compounds will be examined; namely $LaCl_3$:Pr^{3+}, $LiYF_4$:Pr^{3+} and $CsCdBr_3$:Pr^{3+}. The praseodymium ion common to all has $N = 2$, *i.e.* two electrons in the unfilled $4f$ shell, making it a non-Kramers ion. Most of their spectra are adequately explained by ordinary CF analysis, but the $^1G_4$ and $^1D_2$ multiplets are not [5, 11]. The difference is particularly bad with $LiYF_4$:Pr^{3+}, so this compound and the $^1D_2$ multiplet shall be treated in greater specific detail.

These multiplets are shown in figure 1.1 where energies are given in units of wavenumbers (reciprocal centimeters) with respect to the (compound dependent) $4f^2$ ground state level. All numerical values specified within this chapter, be they matrix elements, uncertainties, RMS errors or energies shall be in the same units. Experimental data is incomplete and the lines shown originate from $LiYF_4$:Pr^{3+} numerical calculations but their general location and multiplet positioning does not appreciably change with different crystal hosts. Multiplets are named according to the spectroscopist's $^{2S+1}L_J$ convention, where the letters S,P,D,F,G,H,I correspond to numerical values 0,1,2,3,4,5,6 of L.

Sections 1.2, 1.3 and 1.4 describe Hamiltonian reduction theory, its matrix algebra form and its application to an EBS Hamiltonian. Section 1.5 then presents an overview of CF, CCF and EBS parametrisations of experimentally determined spectral lines, briefly describing the operators and merits of each method. Section 1.6 deals with fitting CCF operators to a model EBS Hamiltonian created with the previous reduction technique. This allows an expansion of configuration effects in

terms of correlation operators and a comparison of parameters from the two methods. Finally, brief conclusions are drawn in section 1.7.

Figure 1.1: Energy level structure of Pr^{3+} in $LiYF_4$

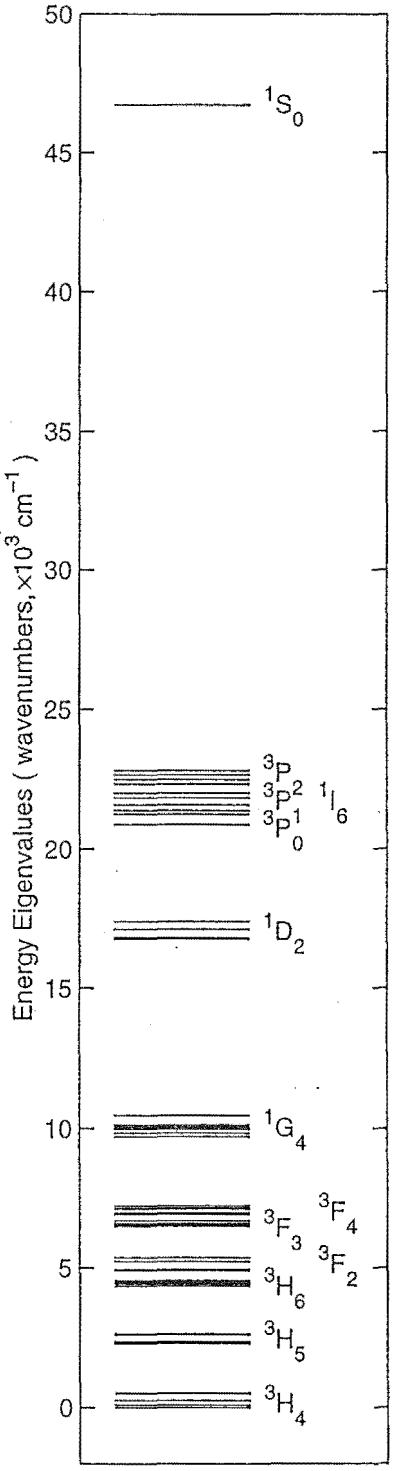

1.2 Matrix Reduction and Model Spaces

There exist several recipes whereby large Hamiltonians may be reduced to lower dimension without loss of information regarding eigenvalues and eigenvectors of those states retained in the reduced space. In the jargon of the field, the large Hamiltonian is termed an initial or full Hamiltonian and the smaller reduced Hamiltonian either the effective or model Hamiltonian. Exhaustive papers and books [14, 15, 23] on the reduction process and operator algebra of such effective Hamiltonians have been published, from which the method presented here is drawn. Related perturbation theory is treated with a diagram formalism in [16] and algebraically in [2], but shall not be required here.

The procedure begins with a Hamiltonian H having a full spanning set F of orthonormal eigenvectors, consisting of a system subset S to be retained and an environment subset E to be discarded. Typically S will correspond to some particularly interesting physical arrangement, the $4f^2$ electronic configuration for instance, and E to all other configurations, $4f6p$ and the like. All states of E are lost during the reduction along with the information they carry, most notably their eigenvalues. States within S get projected into a smaller vector space in such a way as that their orthonormality and eigenvalues are unchanged. This is done indirectly, by performing certain operations upon S and using the results to generate a model Hamiltonian M which describes S in the reduced vector space. Due to the dimensionality change in going from full to model space, the corresponding representations of states in S must differ even though the states themselves remain unchanged.

The use made of effective Hamiltonian theory here is rather different to its most common employment. Within this volume, the initial Hamiltonian is always known as will be the crystal field operators for the reduced space. Physical chemists have no such luxury, and perform calculations in order to find effective operators for the molecule studied without having knowledge of the full universal Hamiltonian. An effective Hamiltonian can then be formed as a sum of effective operators in the same way as crystal field Hamiltonians are defined. Examples of such calculations are given in [25] and [40].

Returning to the immediate reduction type of problem, *i.e.* to discard a set of states E from a Hamiltonian without altering the others, it has been shown that the majority of reduction methods will lose either eigenvector orthonormality or Hamiltonian Hermiticity in the course of preserving eigenvalues [14]. The technique which will be considered here yields a canonical model Hamiltonian $\tilde{\mathrm{M}}$, meaning

one which is Hermitian and so has a spanning set of orthonormal eigenvectors. The net result is equivalent to retaining the effect of interactions between S and E states upon the S states, but without having to consider the E states themselves.

When there are no $S \rightleftharpoons E$ interactions, the reduction process becomes trivial as F block-diagonalises into the direct sum $S \oplus E$ with S and E independent. For this case, E is simply discarded and the model space eigenvectors are the full space representations of S truncated by removing as many zeroes as the dimension of E. Similarly, the canonical model Hamiltonian is obtained by block-diagonalisation of the full Hamiltonian, and discarding the E component and the (zero valued) $S \rightleftharpoons E$ cross terms. In practice, such truncations are performed routinely whenever the rest of the universe is ignored and the system is considered to be isolated. This is the approach taken with CCF analysis which assumes that excited configurations are insignificant with regard to observed spectra.

Now consider a non-trivial Hamiltonian where the presence of $S \rightleftharpoons E$ interactions means that $F \neq S \oplus E$. Eigenvectors of the S and E states become intimately mixed with each containing components of the other set's basis states. Consequently the environment states cannot be ignored or conveniently forgotten, and the canonical reduction procedure must be called upon.

To begin, let S contain states represented $|\alpha\rangle$ and the model space representations of these same states be $|\alpha_0\rangle$. In other words $|\alpha\rangle$ are the exact system eigenfunctions of the full Hamiltonian $\mathbf{H}$ and $|\alpha_0\rangle$ the as yet unknown reduced Hamiltonian eigenfunctions. Furthermore denote the states of E by $|\beta\rangle$ and, of course, there are no model space analogues for these. Projection operators for full and model space can now be defined *viz.*

$$\mathbf{P} \equiv \sum |\alpha\rangle\langle\alpha| \tag{1.4}$$

$$\mathbf{P}_0 \equiv \sum |\alpha_0\rangle\langle\alpha_0| \tag{1.5}$$

$$\mathbf{k} \equiv \sum |\alpha\rangle\langle\alpha_0| \tag{1.6}$$

$$\mathbf{l} \equiv \sum |\alpha_0\rangle\langle\alpha| \tag{1.7}$$

Operators $\mathbf{P}$ and $\mathbf{P}_0$ act entirely within the full and model spaces respectively. The first operates upon both $|\alpha\rangle$ and $|\beta\rangle$, acting as an identity on the former, and returning zero for the latter. The second operator $\mathbf{P}_0$ is really just an identity since the $|\alpha_0\rangle$ span the model space, but with a small adjustment later on, it will turn out to be computationally useful at a midpoint in the procedure part way between the set of $|\alpha\rangle$ and properly orthonormalised $|\alpha_0\rangle$. The last two are projection operators

proper, with $\mathbf{l}$ mapping $|\alpha\rangle$ onto $|\alpha_0\rangle$ and $|\beta\rangle$ onto zero, whilst $\mathbf{k}$ restores $|\alpha\rangle$ from $|\alpha_0\rangle$. These four mappings are related by identities which include the following:

$$\mathbf{k}\mathbf{P}_0 = \mathbf{k} = \mathbf{P}\mathbf{k} \tag{1.8}$$

$$\mathbf{l}\mathbf{P} = \mathbf{l} = \mathbf{P}_0\mathbf{l} \tag{1.9}$$

$$\mathbf{k}\mathbf{l} = \mathbf{P} \tag{1.10}$$

$$\mathbf{l}\mathbf{k} = \mathbf{P}_0 \tag{1.11}$$

Following [14] and [23], a simple model Hamiltonian $\mathbf{M}$ for the states of S in terms of the analogues $|\alpha_0\rangle$ may immediately be defined as equation (1.12) which unfortunately, is non-Hermitian with non-orthogonal eigenvectors. In other words, this is not a canonical model and the $|\alpha_0\rangle$ representations are not orthonormal.

$$\mathbf{M} = \mathbf{l}\mathbf{H}\mathbf{k} \tag{1.12}$$

To obtain a canonical model involves careful choice of $\mathbf{k}$ and $\mathbf{l}$. Despite appearances in equations (1.6) and (1.7), $\mathbf{k}$ does not, in general, equal $\mathbf{l}^\dagger$. However, if this was the case, then equation (1.12) would become of the same form as a similarity transformation and behave rather nicely. Fortunately there is a certain degree of freedom in the choice of the $|\alpha_0\rangle$'s, whilst obeying dimensional constraints, orthonormality conditions and continuing to describe interactions between states within S. This transcribes into freedom of choice for either $\mathbf{k}$ or $\mathbf{l}$, and a standard option is to take

$$\mathbf{l} = \mathbf{P}_0\mathbf{P} \tag{1.13}$$

which satisfies equation (1.9) since $\mathbf{P}\mathbf{P} = \mathbf{P}$ and $\mathbf{P}_0\mathbf{P}_0 = \mathbf{P}_0$ provided that both the $|\alpha\rangle$'s and $|\alpha_0\rangle$'s are orthonormal sets. The first already are, the second are being forced to behave so.

The operator $\mathbf{P}$ is known, so equation (1.10) fixes $\mathbf{k}$ once $\mathbf{l}$ is chosen. Taking $\mathbf{l}^{-1}$ to signify the right-inverse of $\mathbf{l}$ such that $\mathbf{l}\mathbf{l}^{-1} = \mathbb{1}$ (in general $\mathbf{l}^{-1}\mathbf{l} \neq \mathbb{1}$) and right-multiplying on both sides gives

$$\mathbf{k} = \mathbf{P}\mathbf{l}^{-1} \tag{1.14}$$

Yet still $\mathbf{k} \neq \mathbf{l}^\dagger$. Substituting these into equation (1.12) correctly reproduces the eigenvalues of the S eigenvector subset of initial Hamiltonian $\mathbf{H}$ in the model $\mathbf{M}$, but the model's own eigenvectors are not orthonormal and the model is non-Hermitian. However with this definition of $\mathbf{k}$, a new 'canonical' projection operator $\hat{\mathbf{K}}$ may

be defined and used to produce a canonical model Hamiltonian via the preferred similarity-formed transformation [14, 23].

$$\hat{\mathrm{K}} \equiv \mathrm{k}(\mathrm{k}^{\dagger}\mathrm{k})^{-1/2} \tag{1.15}$$

$$\hat{\mathrm{M}} \equiv \hat{\mathrm{K}}^{\dagger}\mathrm{H}\hat{\mathrm{K}} \tag{1.16}$$

Regarding equation (1.12), this is equivalent to $\mathrm{k} = \mathrm{l}^{\dagger}$ as was sought. This canonical model has all the desired properties described; reproduction of eigenvalues and eigenvector orthonormality for the states of S without having to consider E at length, and of course Hermiticity. Eigenvectors of $\hat{\mathrm{M}}$ are denoted $|\hat{\alpha}\rangle$ and the canonical projection operator may be used to restore the original representations $|\alpha\rangle$ from these analogues.

$$\mathrm{H}|\alpha\rangle = \varepsilon|\alpha\rangle \quad \Longrightarrow \quad \hat{\mathrm{M}}|\hat{\alpha}\rangle = \varepsilon|\hat{\alpha}\rangle \tag{1.17}$$

$$\langle\alpha_i|\alpha_j\rangle = \delta_{ij} \quad \Longrightarrow \quad \langle\hat{\alpha}_i|\hat{\alpha}_j\rangle = \delta_{ij} \tag{1.18}$$

$$|\alpha\rangle = \hat{\mathrm{K}}|\hat{\alpha}\rangle \tag{1.19}$$

Eventually this procedure shall be used to transform $4f^2 + 4f6p$ EBS Hamiltonians into purely $4f^2$ models for the purpose of expressing configuration effects in terms of correlation operators. Prior to doing so, some practical considerations must be mentioned.

1.3 Computational Aspects

In order to deal with reality, physicists are obliged to work not in abstract spaces, but with actual numbers, decimal points and all. Regarding the initial Hamiltonian, this invariably means a specific matrix representation with interactions defined against some choice of physical states in an arbitrary ordering. Dimensionality mismatch problems often occur when transcribing the operator algebra of [14] into this form, but are repairable in the method presented here. The CF/CCF $4f^2$ and EBS $4f^2 + 4f6p$ Pr^{3+} Hamiltonians are defined in terms of a two-electron free-ion Russell-Saunders $SLJM$ basis, but the host-crystal field perturbs the Hamiltonian so that these states are no longer eigenstates.

The most straightforward method to form a model Hamiltonian would be to diagonalise the initial, that is rewrite it with respect to its eigenstates, and then discard the unwanted portion in the isolated system approach mentioned previously. The resulting model is Hermitian (diagonal) and has orthonormal eigenvectors with the correct eigenvalues, all as required. Its shortfall is that now the interactions are defined with respect to a different set of states than were the originals. The technique of the previous section does not suffer from this problem, allowing a $4f^2$ basis state model to be calculated from the $4f^2 \oplus 4f6p$ basis full EBS Hamiltonian.

In this case, the initial Hamiltonian is the $4f^2 + 4f6p$ EBS matrix describing configuration interactions between the $4f^2$ states of interest and the excited $4f6p$ levels. Other excitations are not considered in the derivation of this matrix, they fall into the 'rest-of-universe' category from which the Hamiltonian and its states are considered independent, in the same way as CCF analysis ignores the $4f6p$ configurations.

It is found to be computationally faster and more precise to block-diagonalise the initial Hamiltonian matrix H into n independent sub-Hamiltonians or blocks H_j indexed by integer variable $j \in \{1, 2 \ldots n\}$. Each sub-Hamiltonian may be treated separately, and doing so reduces the total number of floating point operations required for the reduction. This translates into accurate eigenvectors, less numerical noise in the form of rounding errors, and zeroes which are actually zero instead of 10^{-12} or thereabouts. Block-diagonalisation can be achieved either by a sorting routine acting upon the state ordering convention used in the Hamiltonian definition, or equivalently by a similarity transformation. Neither process requires any floating point operations in itself.

Figure 1.2: Block-diagonalisation

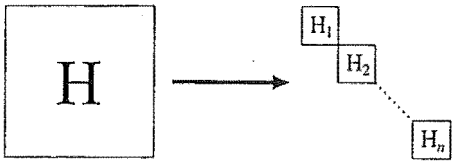

A closer inspection of each sub-Hamiltonian reveals three classes of matrix elements. Those associated only within the desired system states S, those with only the unwanted environmental states E, and cross-terms X betwixt the twain. It is when the cross terms are zero that block-diagonalisation is possible and the matrix can be broken up into separate parts. Consequently the cross-terms here cannot all be zero, or else the S and E components would have formed separate blocks.

Figure 1.3: Matrix components

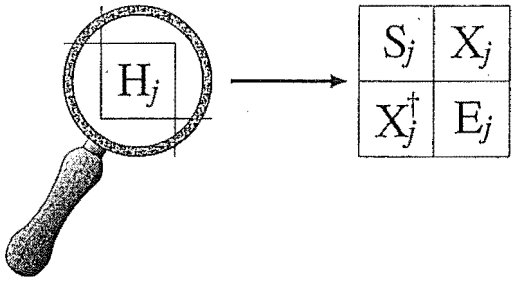

Each block is now treated separately. The eigenvectors are found and form a square matrix V of column vectors with the same dimensions as the parent sub-Hamiltonian. From this matrix the eigenvectors belonging to the S states are extracted into a second matrix V_S. This is actually rather subtle, the eigenvectors are not the same as the basis vectors used in defining H and which actually constitute S. What is done, is the eigenvalues of H are found and associated with unique basis states, the true eigenvalues for which are the known free-ion energy levels, under the free-ion Hamiltonian. The idea is that the eigenvalues and eigenvectors of H arise from crystal perturbation of the free-ion energy levels, making it possible to say "this eigenvalue of H is close to this free-ion level, so that the corresponding H eigenvector is associated with perturbation of whichever basis state". In practice the assignments also have to consider multiplets, degeneracies and sometimes polarisation data, and might be regarded as more of a theology than a science [6].

Figure 1.4: Eigenvector extraction

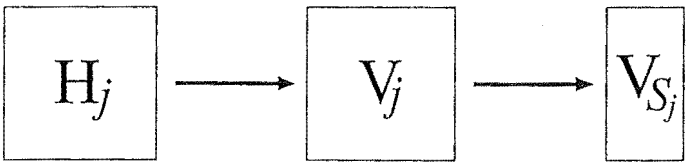

Once the association between eigenvectors and basis vectors has been made, the filtering process in going from V to V_S can be accomplished by sorting the columns of V by eigenvalue. This is allowed, since it turns out that the ordering of eigenvectors within V and V_S makes absolutely no difference to the form of the final canonical model Hamiltonian. If the eigenvalues of V_S are known to be say, numbers x, y and z of V when put in ascending order, then those columns can be easily picked out. More generally, the operator P_0 is put into matrix form.

$$\{P_0\}_{ij} \equiv \begin{cases} 1 & \text{iff } |\alpha_{0i}\rangle = |\alpha_j\rangle \\ 0 & \text{otherwise} \end{cases} \tag{1.20}$$

Where $|\alpha_{0i}\rangle$ is the i^{th} model state of V_S, identified as representing the j^{th} original state $|\alpha_j\rangle$ of V. This isn't quite the same definition of P_0 as given previously (1.5), and behaves not unlike $\mathbf{k}$ (see figure 1.6). It comes from needing to be able to write something down as a numerical matrix to form equation (1.13). Essentially, the representations of the model space analogues $|\alpha_0\rangle$ have been (temporarily) taken as identical to the representations of the full space states $|\alpha\rangle$, dimensionality considerations be damned.

Now P_0 is as deep as V_S is wide and at least this width up to the dimension of V, the actual size being dependent upon the state ordering convention. This would prevent forming P_0P except that the problem is readily overcome by appending columns of zeroes onto P_0 until the width is the same as for V. The whole construct is now called P_0, replacing the earlier form, and is used for the V_S selection procedure as shown overleaf.

Figure 1.5: Correcting the dimensions of P_0

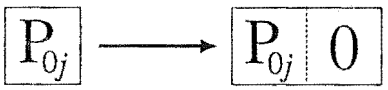

Figure 1.6: Selecting V_S with P_0

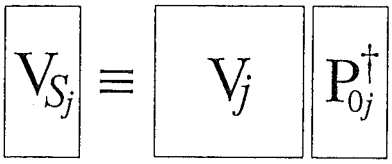

The column vectors of V_S constitute a representation of the set of eigenkets $|\alpha\rangle$, and the matrix form of **P** is defined as per equation (1.4).

Figure 1.7: Projection matrix P

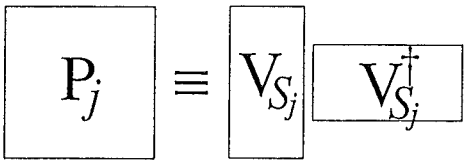

Figure 1.8: P acting on V

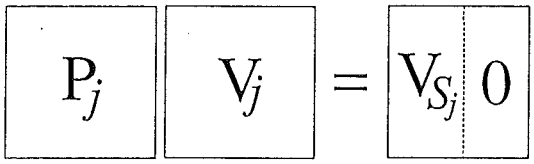

Now the matrix equivalent of l can be formed by equation (1.13). The process simply discards those rows of P for which the equivalently numbered row of V is associated with an eigenvalue of an unwanted vector from E. When the state convention has been chosen such that all the system eigenvectors lie together at the left side of V, the matrix operation is identical to truncation of P.

Figure 1.9: Defining l from P and P_0

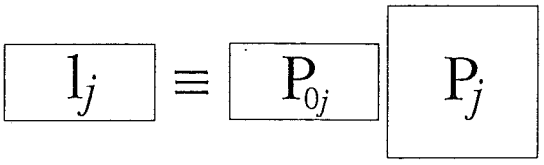

Figure 1.10: Truncation of P into l

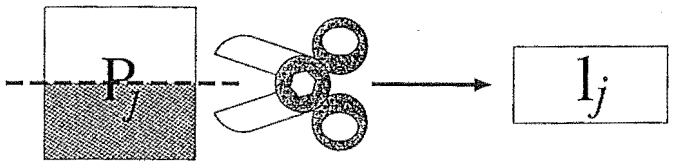

The matrix for k is obtained as per equation (1.14) so that the choice of k and l here are consistent with equations (1.10) and (1.11), and the original operator definitions (1.6) and (1.7). Calculations were performed in MATLAB which supports matrix division to mean "right-multiply by the right-inverse of", and that notation is adopted here.

Figure 1.11: Matrix division for k

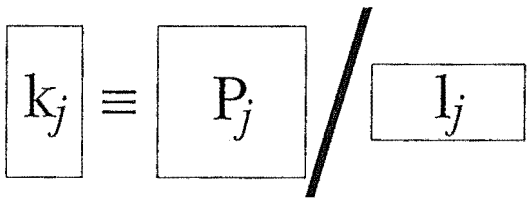

Formation of the canonical projection matrix and canonical model Hamiltonian is carried out exactly as per the operator formulation of equations (1.15) and (1.16).

Figure 1.12: Canonical projection operator

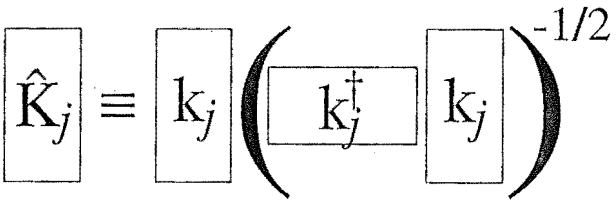

Figure 1.13: Sub-Hamiltonian canonical model

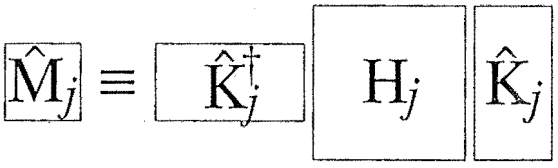

Lastly the model Hamiltonians for all blocks are reassembled into a block-diagonal matrix. The state ordering convention for each is known, and with the ordering of the blocks themselves gives the convention for the entire matrix. With this information it is simple to shuffle the block-diagonal form into any other, and usually this will be the chosen to match that of the S component of the original Hamiltonian H.

Figure 1.14: Reassembly of independent sub-models

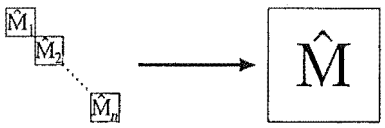

Should it be required, exactly the same sorting procedure performed on the block-diagonalised $\hat{K}_j$ matrices yields an overall $\hat{K}$. Hence there exists a similarity-formed transform from the full Hamiltonian H into the canonical model M for any state ordering convention of the latter.

Figure 1.15: Reassembly of $\hat{K}$ matrices

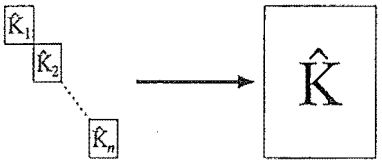

Figure 1.16: One step similarity-formed transformation

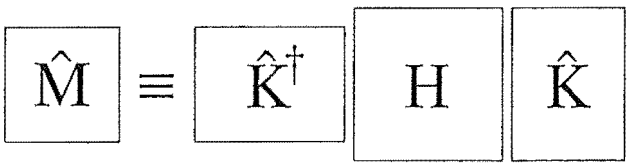

With the reduction procedure now expressed in matrix form, application to a numerical EBS Hamiltonian is straightforward.

1.4 Application to the Crystal Field

Within the chosen Russell-Saunders basis there are 91 $4f^2$ basis states and 84 $4f6p$ basis states for the Pr^{3+} $4f^2$ configuration. These basis states are the free-ion Russell-Saunders $|SLJM\rangle$ eigenstates which are clearly not going to be eigenstates for the crystal field perturbed centre. On application of the matrix reduction recipe to the 175 state $4f^2+4f6p$ EBS $LaCl_3$:Pr^{3+}, $LiYF_4$:Pr^{3+} and $CsCdBr_3$:Pr^{3+} Hamiltonians, CCF sized 91 state $4f^2$ space canonical models are obtained, being defined in terms of the same basis functions as are the CCF operators. These retain all $4f^2$ state information present in the EBS Hamiltonians and consequently the only data loss is for the $4f6p$ states which are not experimentally observed, their energies being too high. Eigenstates of the CCF and model EBS Hamiltonians exist within the same space and by fitting CCF operators to the EBS model, it becomes possible to do a comparison of the fitted parameters for the CCF and (reduced) EBS matrices.

The real-valued EBS Hamiltonian is shown in figure 1.17, and can be divided into four sections by basis state. The ff component contains matrix elements of the form $\langle 4f^2|\mathbf{H}|4f^2\rangle$, the fp component $\langle 4f^2|\mathbf{H}|4f6p\rangle$ *etc.* After reduction, the canonical EBS model is expressed entirely in terms of ff basis states, but fp and pp effects upon these are retained by the model. The ff model, it should be noted, is not the same as the full EBS ff component section.

Figure 1.17: Initial EBS Hamiltonian

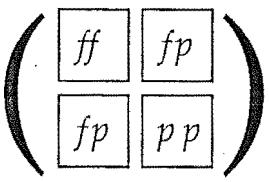

The idea is to take extended basis set configuration interaction crystal field (EBS) and correlation crystal field (CCF) parameterisations of some physical system, form the EBS Hamiltonian as sum of parameters times operators, reduce it to the same set of basis states as the CCF Hamiltonian, and then fit CCF operators to the reduced EBS model. This allows an evaluation of EBS effects in terms of CCF interactions.

1.5 Crystal Field Analysis

This section deals with CF, CCF and EBS parametrisations of experimental data and not with fitting CCF operators to an EBS model Hamiltonian.

Tables 1.2, 1.3 and 1.4 display fitting results for three praseodymium doped halide lattices, specifically $LaCl_3$, $LiYF_4$ and $CsCdBr_3$. Praseodymium centres within these crystals have site symmetries of C_{3h}, S_4 and C_{3v} respectively, however the $LiYF_4$:Pr^{3+} centres can be approximated as D_{2d} which is done in order to simplify numerical operator generation. The first two parameters E_{AVG} and $F^0(ff)$ are both associated with diagonal matrix operators representing the average electrostatic force upon the $4f^2$ states and shift the energy of the entire $4f^2$ configuration. They differ in that the matrix associated with parameter E_{AVG} has been scaled so that its elements are all unity valued, whilst the $F^0(ff)$ operator has not. Otherwise, parameter names are the conventional ones used in all the literature [4, 9, 13, 33]. Operators F^2, F^4 and F^6 are electrostatic single-electron Slater (or Slater-Condon) interactions, Coulombic two-electron interaction parameters are denoted by α, β and γ, and $\zeta(f)$ is a spin-orbit coupling constant [9]. The CF column lists parameter values obtained by fitting standard crystal field operators to experimentally determined energy levels. Similarly, the EBS and CCF columns give results for extended basis set configuration interaction crystal field and correlation crystal field parameterisations of the same experimental data.

CF and CCF results have been taken from [5]. In the case of $LiYF_4$:Pr^{3+} these are fits to the experimental energy levels used for [17], the main sources for which are [10] and [35]. An EBS $LiYF_4$:Pr^{3+} parameterisation has also been published [11], but this is based upon the experiments of [10] and [24]. Consequently the CCF fit in [5] and the EBS fit in [11] are to slightly different sets of data. Such differences arise because experimental energies may be inaccurate or uncertain, and sometimes no measurement has been made since some lines lie outside of convenient optical ranges ($0 - 40000\,\text{cm}^{-1}$ at most) [11]. Spectra are generally taken with polarised beams, in which there is a choice of type, and the temperature can be anywhere between 10 and 300 Kelvin [10]. Different techniques are available for performing the measurements, emission versus absorption for instance, with some considered more accurate than others, and conflicting published values do result. Each level must also be assigned to a specific multiplet, and these often vary between publications. In short, the measurements, energy determinations and multiplet assignments are not simple tasks.

When it comes to choosing lines for a fitting data set, a certain amount of discretionary judgement seems to be applied in deciding which lines to include as experimental data and which to discard. More importantly, the numerical conditions and procedures used in the CCF and published EBS fits are significantly different. This is at odds with the immediate objective which requires exactly the same data and conditions be used in each case to be able to make a useful comparison of parameters.

All the EBS columns here are reproduced from unpublished results (see acknowledgements) that were fitted to exactly the same data as used for the CF and CCF columns [5], and with the fitting conditions held as closely as possible to those of the CCF fits as allowed by the different formulation. The exact conditions are:

- The Marvin integrals for spin-spin and spin-other-orbit effects are held in fixed ratios suggested by relativistic Hartree-Fock calculations [9].

$$M^2 = \tfrac{14}{25}M^0 \qquad M^4 = \tfrac{19}{50}M^0$$

- The two-electron electrostatically correlated magnetic parameters are also held in fixed ratios according to the same analysis [9].

$$P^4 = \tfrac{3}{4}P^2 \qquad P^6 = \tfrac{1}{2}P^2$$

- $LiYF_4$:Pr^{3+} D_4^4/D_0^4 ratio held fixed at B_4^4/B_0^4 ratio.
- $CsCdBr_3$:Pr^{3+} D_3^4/D_0^4 ratio held fixed at B_3^4/B_0^4 ratio.
- All values in square brackets are held absolutely fixed.

Values for the parameters in columns CF, EBS and CCF are obtained by an iterative non-linear least squares procedure. What is actually done, is that trial parameters are put in, a Hamiltonian is formed by summing over the parameter scaled operators and then the eigenvalues of this Hamiltonian are compared against the experimentally determined levels. By variation of parameters, a Hamiltonian is found whose eigenvalues match experiment as closely as possible and the corresponding parameter values taken as the best estimates. Uncertainties of the free parameters are given in round brackets, but it does not follow that the uncertainties in parameters held at fixed ratio to these scale the same way. Error estimates for the EBS parameters were unavailable. In general, adding more parameters to a fit always improves it, but beyond a certain number of free parameters the parameter values themselves become uncertain.

If a system of equations is to have a unique solution, there must be at least as many independent equations as there are variables to be determined. The same constraint applies here, any attempt to fit more free parameters than there are energy levels leads to multiple solutions and undetermined parameters. Often a fit of equally many operators as spectral lines, or even of slightly fewer, will produce huge uncertainties that can be larger than the parameters themselves. This forces the number of operators in any fit to be kept lower than the number of states, but in practice such a small number of interactions is inadequate to accurately describe the total Hamiltonian, as witnessed by relatively poor reproduction of the energies. Increasing the number of operators allows more different interactions to be accounted for, but as the number approaches that of the spectral lines, the aforementioned problems arise.

A compromise is to find parameters which are predicted to remain in some fixed predetermined ratio, regardless of their actual values, just as for the Marvin parameters above. This effectively allows a large number of interactions to be included in the Hamiltonian whilst retaining a small set of free parameters. Provided that the fixed ratios are accurate there is no real loss in overall precision, but if they are poor then there will be no gain at all.

The conventional CCF Hamiltonian (1.3) is formulated in terms of $\mathrm{g}_{iq}^{(k)}$ two-electron spin-independent operators. There are far too many of these to possibly include them all in a fit to experimental lines where there might typically be only forty to sixty data points. Consequently what has been done in the CCF results here, is that rather than fitting the $\mathrm{g}_{iq}^{(k)}$'s themselves, the parameterisation is performed in terms of compound operators $\delta_q^{(k)}$ and associated parameters D_q^k in an analogous summation;

$$\mathrm{H}_{CCF(\delta)} = \sum_{kq} D_q^k \delta_q^{(k)} \tag{1.21}$$

The operators of this "delta-function" model based upon [18] are defined as sums of the $\mathrm{g}_{iq}^{(k)}$ operators [5, 18, 32]. Hence fitting the $\delta_q^{(k)}$'s is equivalent to fitting one of the $\mathrm{g}_{iq}^{(k)}$'s in each sum whilst holding the others at the appropriate ratio to it. The physics behind this model lies in the filled $5s$ and $5p$ shells which extend further into the crystal lattice than do the $4f$ levels and partially shield these electrons from the crystal field. Ãs such, the electromagnetic interaction between the $4f$ electrons and the crystal falls off much faster with distance than would otherwise be expected. This allows an approximation to be made by assuming that interactions occur only when the electrons are localised at the position of the crystal ligand, hence the name

of delta function. Equations (1.22) and (1.23) give the exact delta function model operator definitions for the cases $k = 2$ and $k = 4$.

$$\delta_q^{(2)} \equiv \frac{35\sqrt{7}}{3\sqrt{2}} \mathrm{g}_{2\,q}^{(2)} - \frac{35\sqrt{7}}{\sqrt{22}} \mathrm{g}_{3\,q}^{(2)} - \frac{28\sqrt{105}}{\sqrt{143}} \mathrm{g}_{10\,q}^{(2)} \tag{1.22}$$

$$\delta_q^{(4)} \equiv -\frac{21\sqrt{105}}{2\sqrt{11}} \mathrm{g}_{2\,q}^{(4)} + \frac{63\sqrt{105}}{22} \mathrm{g}_{3\,q}^{(4)} + \frac{84\sqrt{42}}{\sqrt{715}} \mathrm{g}_{10A\,q}^{(4)} + \frac{8232\sqrt{3}}{11\sqrt{1105}} \mathrm{g}_{10B\,q}^{(4)} \tag{1.23}$$

There are analogous equations for $k = 6, 8, 10, 12$ but these operators are not used in any of the parametrisations given here. Historically the $\mathrm{g}_{i\,q}^{6}$'s, the next symmetry allowed k values, have been left out as they are found to not significantly improve the fit to experimental data over the standard (up to $k = 4$) delta-function model [5] due to the approximate $\mathrm{D_{2d}}$ site symmetry. All $G_{i\,q}^{k}$ parameters shown in tables 1.2, 1.3 and 1.4 have been calculated from the given D_q^k parameters by these equations. It is the D_q^k parameters which are actually determined in fitting to experimental data, the $\mathrm{g}_{i\,q}^{(k)}$ operators are not used. Therefore, to form a Hamiltonian from these tables by summing parameters times operators use either the $G_{i\,q}^{k}$'s or equivalent D_q^k's but not both.

In addition to the parameters listed in these three tables, there are several others associated with each EBS fit. All are free-ion parameters, independent of the crystal compound, and have been separated out into table 1.1 so that the others will fit on the page. The F^0 parameter's associated operator is an energy shift between the $4f^2$ and $4f6p$ states. Next, the $\zeta(p)$ operator has the same function as $\zeta(f)$, only for $4f6p$ rather than $4f^2$ states. The R^n operators represent components of a $1/r$ Coulombic potential. For instance, $\mathrm{R}^2(ff, fp)$ and $\mathrm{R}^4(ff, fp)$ are interactions between states in the ff $(4f^2)$ and fp $(4f6p)$ groups, being respectively identified as the dipole and quadrupole terms in expansions of radial integrals with the form $\langle ff|\frac{e^2}{\mathrm{r}_{12}}|fp\rangle$.

Each parameter table from 1.2 to 1.4 ends in a set of six fitting statistics, the last three of which apply only to the CFE column which will be dealt with in the next section. Of the remainder, N is the number of experimental levels, *i.e.* data points, that were used for the fit. The σ's are RMS errors in wavenumbers between energy levels predicted by the fitted Hamiltonian, and those of the experimental data. Only those N fitting levels are used to calculate RMS errors, even when additional data is available but was not used for fitting. Each degenerate level is considered as one, not two, data points for both N and RMS purposes since they are not independent. Plain σ is calculated over all this data whilst $\sigma(^1\mathrm{D}_2)$ is for the $^1\mathrm{D}_2$ multiplet levels only.

Table 1.1: Additional EBS parameters

Parameter	Value
$F^0(fp) - F^0(ff)$	124343
$\zeta(p)$	[3800]
$R^2(ff, pp)$	11576
$R^2(fp, fp)$	3249
$R^4(fp, fp)$	2973
$R^2(ff, fp)$	−4886
$R^4(ff, fp)$	−2968

In the case of $LaCl_3:Pr^{3+}$, the overall fitting precision, as witnessed by the RMS error σ, is little improved in going from old style CF fitting to either EBS or CCF. The $^1D_2$ multiplet fitting, which has historically been singled out [5], as generally this is the least well CF fitted individual multiplet, is much improved though. Likewise $CsCdBr_3:Pr^{3+}$ behaves similarly except that only the CCF method improves $^1D_2$ fitting. In the case of the lower symmetry $LiYF_4:Pr^{3+}$, both overall and $^1D_2$ fitting is very much improved with the more advanced techniques.

Table 1.5 provides a more detailed multiplet by multiplet breakdown of the RMS errors between fitted and observed energy levels. The total number of states for each multiplet is given in round brackets, and does not depend upon the crystal host. Columns N are the number of energy levels (data points) used for fitting purposes from each multiplet. These are generally lower than the number of states due to compound dependent degeneracies or lack of experimental data, the quality of which deteriorates from left to right across the table. Degeneracy reduces the number of available data points since only differently valued energies can be used. The amount of degeneracy varies from compound to compound according to the symmetry. For instance the $^1D_2$ multiplet has two degenerate pairs in $LaCl_3:Pr^{3+}$ and $CsCdBr_3:Pr^{3+}$ leaving three data points from five states, but with $LiYF_4:Pr^{3+}$ the lower symmetry causes one of the pairs to become split, providing four distinct lines.

Also for $LiYF_4:Pr^{3+}$, 48 energy levels have been experimentally determined, but the two $^3P_1$ lines exhibit unusually small crystal field splitting which cannot be accounted for by CCF analysis [5] and were subsequently removed from the parameterisation data set. The resulting 46 levels are an insufficient number to determine all the atomic parameters which is why several have been held fixed at values close

to those of LaF_3:Pr^{3+} [5, 6]. Although in general parameter $B_4^6(ff)$ has an imaginary component, this was found to be statistically insignificant and omitted from the calculations [5].

An examination of the parameters in the tables 1.2, 1.3 and 1.4 shows broad similarities between the free-ion parameters of all three methods in all three compounds. Crystal field parameters $B_q^{(k)}(ff)$ tend to match rather less well, although the CCF values are usually closer to the CF than are those of the EBS fit. This is largely due to the way in which the operators are defined. A CF operator is defined with respect to a purely $4f^2$ basis set, and is the best single low-energy electron approximation to the behaviour of the Pr^{3+} ion. The CCF parametrisation also features operators defined on this basis set and the only reason a given CCF parameter differs from the corresponding CF value is that the additional $g_{iq}^{(k)}$ or $\delta_q^{(k)}$ operators are not orthogonal to the earlier CF terms over the limited data set of the fit. This causes some of the parameter to be swapped between the CF operator and some combination of CCF operators.

However the most widely accepted physical reason for the poor quality of CF fits is a breakdown of the CF one electron low-energy approximation. Although both correlation and configuration effects undoubtedly have some impact upon $4f^2$ energy levels, it is suspected that electrons are being excited into $4f6p$ states and that these configuration interactions are the major reason behind CF discrepancies. A problem with the EBS approach is that it requires definition of operators on a larger extended basis set, namely $4f^2 \oplus 4f6p$, and a consequence is that the EBS operator complementary to parameter F^2, $B_0^2(ff)$, or whatever is not the same as the corresponding CF and/or CCF matrix. So really there is no sense in directly comparing EBS parameters with CF or CCF results.

But CCF calculations are in many ways easier to work with than EBS, and certain EBS parameters, $F^0(fp) - F^0(ff)$ for instance, are difficult to determine and can cause disproportionately large undue problems. It would be useful to be able to perform CCF fitting and then be able to convert the results back into EBS parameters and vice versa, which is loosely the topic of the next section. By reducing the EBS Hamiltonian to a $4f^2$ model which retains all the configuration effects upon the $4f^2$ states, it is possible to fit CCF operators to this model, as opposed to experimental data, and arrive at an expansion for the configuration effects in terms of correlation operators.

Table 1.2: $LaCl_3$:Pr^{3+} fitting results

Parameter	CF	EBS	CFE	CCF
E_{AVG}	9931(1)		9930	9931(1)
$F^0(ff)$		12179		
F^2	68440(12)	68441	68440	68441(10)
F^4	50183(37)	50230	50170	50170(31)
F^6	32973(19)	33023	32970	32980(17)
α	22.8(0.1)	22.4	22.8	22.8(0.3)
β	−681(8)	−683	−681	−680(7)
γ	1453(7)	1471	1451	1453(6)
$\zeta(f)$	749(1)	750	749	749(1)
M^0	1.81(0.15)	1.82	1.82	1.81(0.12)
M^2	1.01	1.02	1.00	1.01
M^4	0.69	0.69	0.70	0.69
P^2	235(26)	233	234	237(22)
P^4	176	175	176	178
P^6	118	117	115	119
$B_0^2(ff)$	104(6)	197	110	97(6)
$B_0^4(ff)$	−337(14)	−284	−371	−343(13)
$B_0^6(ff)$	−653(20)	−715	−665	−663(17)
$B_6^6(ff)$	447(13)	437	437	445(11)
G^2_{20}			9.2	−20
G^2_{30}			−7.9	18
G^2_{100}			107	22
G^4_{20}			−161	−149
G^4_{30}			114	135
$G^4_{10\,A0}$			425	94
$G^4_{10\,B0}$			414	179
D_0^2				−0.9(1.3)
D_0^4				4.6(1.0)
$B_0^2(fp)$		1764		
$B_0^4(fp)$		[−11000]		
N	60	60		60
σ	6.8	6.2		5.7
$\sigma(^1D_2)$	17.2	9.9		6.6
$\sigma(H)$			2.7	
$\sigma(H_D)$			3.2	
$\sigma(E_{val})$			3.3	

Table 1.3: $LiYF_4:Pr^{3+}$ fitting results

Parameter	CF	EBS	CFE	CCF
E_{AVG}	10203(5)		10209	10204(3)
$F^0(ff)$		12638		
F^2	68979(57)	69227	69145	69025(41)
F^4	50619(154)	50784	50634	50580(109)
F^6	33276(127)	33625	33456	33326(91)
α	[23.0]	[23.0]	23.8	[23.0]
β	−637(30)	−670	−680	−649(21)
γ	[1371]	1369	1340	[1371]
$\zeta(f)$	750(3)	751	749	750(2)
M^0	[2.00]	[2.00]	1.99	[2.00]
M^2	[1.12]	[1.12]	1.07	[1.12]
M^4	[0.76]	[0.76]	0.79	[0.76]
P^2	220(96)	206	210	215(68)
P^4	165	155	161	161
P^6	100	103	100	108
$B_0^2(ff)$	433(41)	178	524	542(48)
$B_0^4(ff)$	−1068(72)	−783	−1174	−1093(51)
$B_4^4(ff)$	1319(44)	990	1423	1327(32)
$B_0^6(ff)$	−67(77)	−327	−60	−45(55)
$B_4^6(ff)$	1187(60)	1534	1128	1165(42)
G_{20}^2			−161	−347
G_{30}^2			141	314
G_{100}^2			345	381
G_{20}^4			−274	−285
G_{24}^4			333	347
G_{30}^4			204	258
G_{34}^4			−267	−314
$G_{10\,A0}^4$			628	179
$G_{10\,A4}^4$			−782	−218
$G_{10\,B0}^4$			626	343
$G_{10\,B4}^4$			−760	−417
D_0^2				−15.9(5.5)
D_0^4				8.8(1.6)
D_4^4				−10.7
$B_0^2(fp)$		4377		
$B_0^4(fp)$		−11411		
$B_4^4(fp)$		14428		
N	46	46		46
σ	22.6	10.6		15.5
$\sigma(^1D_2)$	40.6	10.9		10.8
$\sigma(H)$			6.3	
$\sigma(H_D)$			4.6	
$\sigma(E_{val})$			7.4	

Table 1.4: $CsCdBr_3:Pr^{3+}$ fitting results

Parameter	CF	EBS	CFE	CCF
E_{AVG}	10051(8)		10047	10050(8)
$F^0(ff)$		12638		
F^2	67487(60)	67538	67463	67477(57)
F^4	49587(260)	49544	49465	49581(249)
F^6	32671(158)	32722	32627	32689(153)
α	23.8(0.6)	23.1	23.4	23.6(0.6)
β	[−682.98]	[−682.98]	−690	[−682.98]
γ	[1422]	[1422]	1414	[1422]
$\zeta(f)$	744(3)	745	744	744(3)
M^0	1.4(0.5)	1.35	1.35	1.5(0.5)
M^2	0.8	0.76	0.73	0.8
M^4	0.5	0.51	0.53	0.6
P^2	[200]	[200]	203	[200]
P^4	[150]	[150]	154	[150]
P^6	[100]	[100]	99	[100]
$B_0^2(ff)$	−158(30)	−51	−167	−203(43)
$B_0^4(ff)$	−1192(62)	−1140	−1149	−1115(71)
$B_3^4(ff)$	1367(34)	1711	1365	1393(33)
$B_0^6(ff)$	362(73)	664	364	381(73)
$B_3^6(ff)$	271(45)	343	249	266(43)
$B_6^6(ff)$	39(53)	110	21	2(53)
G^2_{20}			43	205
G^2_{30}			−38	−186
G^2_{100}			−53	−225
G^4_{20}			−133	−88
G^4_{23}				−109
G^4_{30}			105	79
G^4_{33}				−99
$G^4_{10\,A0}$			498	55
$G^4_{10\,A3}$				−69
$G^4_{10\,B0}$			464	105
$G^4_{10\,B3}$				−132
D_0^2				9.4(6.7)
D_0^4				2.7(1.5)
D_3^4				−3.4
$B_0^2(fp)$		−1126		
$B_0^4(fp)$		−14547		
$B_3^4(fp)$		10307		
N	40	40		40
σ	11.1	10.6		10.1
$\sigma(^1D_2)$	10.6	10.9		1.3
$\sigma(H)$			5.1	
$\sigma(H_D)$			1.7	
$\sigma(E_{val})$			7.8	

Table 1.5: Multiplet RMS errors

Multiplet		$LaCl_3:Pr^{3+}$				$LiYF_4:Pr^{3+}$				$CsCdBr_3:Pr^{3+}$			
		N	CF	EBS	CCF	*N*	CF	EBS	CCF	*N*	CF	EBS	CCF
$^3H_4$	(9)	6	6.9	6.9	7.6	5	9	10	4	6	7	9	10
$^3H_5$	(11)	7	7.2	8.0	7.6	6	11	13	12	6	10	10	12
$^3H_6$	(13)	9	2.8	4.3	2.6	8	20	12	19	6	14	14	13
$^3F_2$	(5)	3	6.6	9.1	6.7	3	24	7	27	3	11	9	12
$^3F_3$	(7)	5	4.1	4.0	3.6	5	16	7	16	5	7	7	7
$^3F_4$	(9)	6	5.1	4.7	6.4	7	21	6	14	5	18	10	12
$^1G_4$	(9)	6	8.7	6.7	4.9	5	35	16	20				
$^1D_2$	(5)	3	17.2	9.9	6.6	4	41	11	11	3	11	8	1
$^3P_0$	(1)	1	10.5	10.2	10.9	1	3	2	1	1	11	7	11
$^3P_1$	(3)	2	9.1	9.5	9.4					2	5	8	6
$^1I_6$	(13)	8	2.4	2.5	2.8								
$^3P_2$	(5)	3	3.7	3.1	3.0	2	9	4	2	3	5	6	5
$^1S_0$	(1)	1	0.1	1.6	0.1								
Overall	(91)	60	6.8	6.2	5.7	46	23	11	16	40	11	10	10

1.6 Comparison of Methods

As previously mentioned, a comparison of EBS and CCF parameters as fitted to experimental data is not useful, and so this section deals with fitting CCF operators to the reduced EBS Hamiltonian.

By the method described earlier, the $4f^2 + 4f6p$ EBS Hamiltonian is reduced to a canonical model describing only the $4f^2$ basis states. The model retains all configuration interaction effects of the $4f6p$ states upon states of the model basis, $4f^2$, which is the same as the CCF operator basis. This allows CCF operators to be fitted to the EBS model, giving an equivalent CCF expansion for EBS configuration effects within the $4f^2$ states.

Fits within this section are of CCF operators to the EBS model rather than to experimental data, and the fitting is performed by linear least squares matrix-inversion instead of a non-linear iterative method. All parameters are fitted as free variables. No operators have been held in fixed ratios or at fixed values since here there is a very large number of matrix elements to fit to and none of the problems associated with a limited data set, as when fitting to experimental lines, are present. The consideration here is not with how well either method matches experiment, but to what extent can EBS effects be reproduced with CCF operators.

Columns CFE in tables 1.2, 1.3 and 1.4 give just such CCF Fits to the EBS model as described. The combinations of CCF operators used in these fits have been chosen to match those equivalent to the delta-function CCF fit to experiment. Due to an oversight when numerically generating the operators, there are no G^k_{iq} parameters with $q = 3$ in the CFE table for $CsCdBr_3$:Pr^{3+}.

Again, the numbers are seen as broadly similar, with CFE parameters not quite matching either the comparison CCF or parent EBS values. For CCF this is due to the presence of configuration interactions in the EBS Hamiltonian from which the CFE values are derived. With EBS, the difference is a result of changing from large $4f^2 \oplus 4f6p$ basis operators to the smaller CCF operators.

It is worth noting that CF parameters held fixed in both EBS and CCF calculations, such as α in $LiYF_4$:Pr^{3+} or β in $CsCdBr_3$:Pr^{3+}, do not result in an equivalent CFE parameter of exactly the same value. This is again due to operator differences between EBS and CCF, and holding a parameter at the same value in both cases is clearly not exactly the same condition. When CF parameters have been held in fixed ratios for EBS and CCF, the CFE equivalents, which are all independent, turn out in approximately the same ratio.

CFE columns have three fitting statistics, all RMS errors in wavenumbers as shown, none of which can be directly related to those of the EBS or CCF fits. The first, $\sigma(H)$ is the RMS error between allowed matrix elements over the upper diagonals of the model EBS and fitted CFE Hamiltonians. The latter matrix is formed by summing parameters times operators just as for the CCF and full EBS cases. Only the upper diagonal is used since these real-valued matrices are symmetrical in the leading diagonal and inclusion of the entire matrix would effectively give double weighting to the RMS errors on off-diagonal elements. Allowed matrix elements are those which are not identically zero through some selection rule. In the upper diagonal of these 91-square matrices there are 4186 total elements, but only 1087 of these are allowed. For a graphical depiction of the allowed elements, see figure 1.18 bearing in mind that the actual pattern there depends upon the ordering convention for the matrix basis states $|SLJM\rangle$.

Similarly, $\sigma(H_D)$ is the RMS error between allowed upper diagonal matrix elements within the $^1D_2$ multiplet only. The multiplet contains only five states $|0\,2\,2\,M\rangle$ where M can take on integer values between +2 and −2 inclusive. There are only six allowed elements, five on the diagonal and $\langle 0\,2\,2\,2|\mathrm{H}|0\,2\,2\,-2\rangle$. The third statistic $\sigma(E_{val})$ is the RMS error between the eigenvalues of the CFE and EBS model Hamiltonian matrices. This is calculated across all 91 states which essentially gives double weighting to degenerate levels. All told the highest symmetry centre, $LaCl_3$:Pr^{3+}, has the best match between model EBS and CFE, and the lowest symmetry, $LiYF_4$:Pr^{3+}, the worst.

The objective was to find equivalence relations between sets of EBS and CCF parameters. This would be made much easier with an exact match between the CFE and model EBS matrices. Thus far, CFE fitting has been limited to the same low k valued $\mathrm{g}_{iq}^{(k)}$ operators as used in the CCF delta-function fits, but the defining CCF equation (1.3) is much more general than this. So more of these operators are generated from the Racah-Wigner calculus and incorporated into the CFE parameterisation.

Table 1.6 lists five such sets of results for the compound $LiYF_4$:Pr^{3+}. In the rightmost column, CF, are the parameters from fitting only the nineteen standard crystal field operators. The next column, δ, is exactly the same delta-function $\mathrm{g}_{iq}^{(k)}$ equivalent fit as in table 1.3, and $\delta(6)$ simply includes the $\mathrm{g}_{iq}^{(6)}$ delta-function operators as well. Note that the true delta-function parameters D_q^k are not being fitted, but the set of G_{iq}^k parameters with which they are defined. The δ CCF

parametrisation greatly improves on the CF fit in all respects. As suggested, the $\delta(6)$ CCF set does not significantly improve upon the δ, and in fact the eigenvalue matching becomes worse through a shift in the ground state.

Table 1.6: CFE parameter sets for $LiYF_4:Pr^{3+}$

Parameter	GW	G	$\delta(6)$	δ	CF
E_{AVG}	10209	10209	10209	10209	10209
F^2	69145	69145	69145	69145	69145
F^4	50634	50634	50634	50634	50634
F^6	33456	33456	33456	33456	33456
α	23.8	23.8	23.8	23.8	23.8
β	-680	-680	-680	-680	-680
γ	1340	1340	1340	1340	1340
ζ	749	749	749	749	749
M^0	1.99	1.99	1.99	1.99	1.99
M^2	1.07	1.07	1.07	1.07	1.07
M^4	0.79	0.79	0.79	0.79	0.79
P^2	210	210	210	210	210
P^4	161	161	161	161	161
P^6	100	100	100	100	100
B_0^2	527	527	524	524	519
B_0^4	-1174	-1174	-1174	-1174	-1159
B_4^4	1423	1423	1423	1423	1423
B_0^6	-58.9	-59	-59.3	-60	-60
B_4^6	1128	1128	1128	1128	1128
G_{20}^2	-156	-156	-161	-161	
G_{30}^2	117	116	141	141	
G_{40}^2	-154	-157			
G_{50}^2	73	75.3			
G_{60}^2	6.49	6.49			
G_{70}^2	-13.5	-13.5			
G_{80}^2	-72.7	-71			

Table 1.6: (continued)

Parameter	GW	G	$\delta(6)$	δ	CF
G^2_{90}	32.1	30.5			
G^2_{100}	350	350	345	345	
G^2_{110}	1.31	4.6			
G^4_{20}	-275	-275	-274	-274	
G^4_{24}	333	333	333	333	
G^4_{30}	219	219	204	204	
G^4_{34}	-267	-267	-267	-267	
G^4_{40}	241	245			
G^4_{44}	-303	-303			
G^4_{50}	-136	-140			
G^4_{54}	171	171			
G^4_{60}	-210	-210			
G^4_{64}	260	260			
G^4_{70}	114	114			
G^4_{74}	-143	-143			
G^4_{80}	-40.5	-40.9			
G^4_{84}	43.9	44			
G^4_{90}	14.2	14.6			
G^4_{94}	-15.1	-15.1			
$G^4_{10\,A0}$	621	621	628	628	
$G^4_{10\,A4}$	-782	-782	-782	-782	
$G^4_{10\,B0}$	605	605	627	627	
$G^4_{10\,B4}$	-760	-760	-760	-760	
G^4_{110}	-1.26	-3.73			
G^4_{114}	1.28	1.3			
G^6_{20}	-91.1	-91.2	-91.6		
G^6_{24}	138	138	138		
G^6_{30}	67.6	68	68.5		
G^6_{34}	-103	-103	-103		
G^6_{40}	2.31	2.03			
G^6_{44}	-5.41	-5.43			

Table 1.6: (continued)

Parameter	GW	G	$\delta(6)$	δ	CF
$G^6_{5\,0}$	-0.14	0.14			
$G^6_{5\,4}$	2.51	2.53			
$G^6_{8\,0}$	-27.8	-28.2			
$G^6_{8\,4}$	38	38			
$G^6_{9\,0}$	10.7	11.1			
$G^6_{9\,4}$	-15.8	-15.8			
$G^6_{10\,A0}$	-18.4	-18.4	-21.9		
$G^6_{10\,A4}$	29.4	29.4	29.4		
$G^6_{10\,B0}$	26.5	26.5	26.5		
$G^6_{10\,B4}$	-37.6	-37.6	-37.6		
$G^6_{11\,0}$	0.71	-0.06			
$G^6_{11\,4}$	-2.25	-2.29			
$G^8_{6\,0}$	-0.86	-0.86			
$G^8_{6\,4}$	-0.58	-0.58			
$G^8_{6\,8}$	-0.54	-0.54			
$G^8_{7\,0}$	-0.44	-0.44			
$G^8_{7\,4}$	0.91	0.91			
$G^8_{7\,8}$	-0.77	-0.77			
$G^8_{8\,0}$	-0.56	-0.56			
$G^8_{8\,4}$	-0.25	-0.25			
$G^8_{8\,8}$	0.85	0.85			
$G^8_{9\,0}$	0.44	0.44			
$G^8_{9\,4}$	0.33	0.33			
$G^8_{9\,8}$	-0.53	-0.53			
$G^8_{10\,A0}$	-3.16	-3.16			
$G^8_{10\,A4}$	3.62	3.62			
$G^8_{10\,A8}$	-4.37	-4.37			
$G^8_{10\,B0}$	1.54	1.54			
$G^8_{10\,B4}$	-0.33	-0.33			
$G^8_{10\,B8}$	2.31	2.31			
$G^{10}_{8\,0}$	-0.25	-0.25			

Table 1.6: (continued)

Parameter	GW	G	$\delta(6)$	δ	CF
$G^{10}_{8\,4}$	0.54	0.54			
$G^{10}_{8\,8}$	1.26	1.26			
$G^{10}_{9\,0}$	-0.53	-0.53			
$G^{10}_{9\,4}$	0.56	0.56			
$G^{10}_{9\,8}$	-1.42	-1.42			
$G^{10}_{10\,0}$	-1.91	-1.91			
$G^{10}_{10\,4}$	2.01	2.01			
$G^{10}_{10\,8}$	-1.73	-1.73			
$G^{12}_{10\,0}$	-0.66	-0.66			
$G^{12}_{10\,4}$	0.77	0.77			
$G^{12}_{10\,8}$	-1.23	-1.23			
$G^{12}_{10\,12}$	-0.01	-0.01			
W^{1120}	-5.15				
W^{1220}	0.06				
W^{1320}	5.1				
W^{1340}	-6.49				
W^{1344}	2.57				
W^{1440}	0.02				
W^{1444}	-0.04				
W^{1540}	1.08				
W^{1544}	-2.87				
W^{1560}	0.94				
W^{1564}	4.88				
W^{1660}	0.02				
W^{1664}	0.02				
N	113	100	38	30	19
$\sigma(H)$	0.37	1.1	5.9	6.3	16.1
$\sigma(H_D)$	10^{-11}	10^{-11}	4.6	4.6	39.5
$\sigma(E_{val})$	0.42	1.4	7.6	7.4	24.9

The G column lists all non-zero G^k_{iq} parameters allowed for this system. Symmetry considerations prohibit states with odd angular momentum, and therefore odd values of k and q do not appear. Likewise k, i and q are restricted to a maximum value of $2|M|$ where the angular momentum projection quantum number M cannot exceed ± 6. Moreover, the fourfold symmetry axis of the S_4 Pr^{3+} centre only allows q to take on values which are an integer multiple of four. This version of the CCF operator set significantly improves upon the δ column results, and now the $^1D_2$ matching is exact within the level of numerical noise. A draw-back of course is that now there are 100 operators in the set instead of just thirty.

A complete breakdown of the $^1D_2$ section is given in table 1.7. All parameters from the GW column were fitted to the entire model Hamiltonian, and the resulting scaled $^1D_2$ matrix elements extracted. Parameters not listed in this table made no contribution to this multiplet. The term "magnitude" is meant to indicate a relative contribution from each operator-parameter pair to the $^1D_2$ section of the Hamiltonian. For a given operator, each $^1D_2$ matrix element is multiplied by the parameter to produce the number added to the Hamiltonian in the sum over parameters times operators. The absolute value of each parameter scaled element is taken, and the maximum magnitude is just the largest of these numbers. Average magnitude is calculated by averaging the absolute scaled elements over the $^1D_2$ upper diagonal only. The table is sorted by average magnitude, and it is observed that the fifteen most significant operators on this basis are all included in the delta-function fit.

Absence of $k = 6$ terms is also conspicuous and arises because the $^1D_2$ multiplet has angular momentum $L = 2$, states of which can only be connected with operators of $k \neq 2$ and $k = 4$. Of the five states in this multiplet, two are degenerate leaving only four independent levels, making it possible to get an exact fit with only four suitable operators; say $\mathbf{E}_{\mathrm{AVG}}$ to control the baricentre plus $\mathrm{g}^{(2)}_{10\,0}$, $\mathrm{g}^{(4)}_{10\,A0}$ and $\mathrm{g}^{(4)}_{10\,B0}$ to adjust the splitting. However, this overlooks the necessity to fit the rest of the model Hamiltonian as well, hence the large number of operators in the table.

Returning to table 1.6, it would still be nice to have zero RMS error between the CFE fit and EBS model. The $\mathrm{g}^{(k)}_{iq}$ operators are spin-independent so the next generalisation is to add in spin-dependent one-electron operators $\mathrm{w}^{(SL)JM}$, which are obtained by choosing S and L and coupling these together to obtain J then M. These are still considered CCF operators although they do not appear in the original equation (1.3). There are many of these, but symmetry factors reduce the number which must be considered. In the end, only thirteen have any appreciable signifi-

Table 1.7: Operator magnitudes within the $^1D_2$ multiplet

Parameter	Magnitude	
	Average	Maximum
E_{AVG}	8508	10209
F^2	6048	7257
F^4	3246	3895
F^6	3208	3849
γ	326	392
α	321	385
β	138	167
B_0^4	99	224
B_0^2	74	110
B_4^4	63	378
G^2_{100}	39	58
G^4_{10B0}	33	74
G^4_{10A0}	29	65
G^4_{10B4}	22	129
G^4_{10A4}	19	114
G^2_{40}	7.9	12
G^4_{60}	6.8	15
G^4_{40}	4.9	11
G^4_{30}	4.7	11
G^4_{64}	4.4	27
G^2_{50}	3.8	5.7
G^4_{70}	3.7	8.3
G^2_{30}	3.4	5.2
G^4_{44}	3.2	19
G^4_{34}	3.0	18
G^4_{50}	2.8	6.3
G^4_{74}	2.4	15
G^2_{80}	2.4	3.6
G^4_{54}	1.8	11
G^4_{80}	1.5	3.3
G^2_{90}	1.0	1.6
G^4_{20}	0.9	2.1
G^4_{84}	0.8	4.9
G^2_{20}	0.7	1.1
G^2_{70}	0.6	0.9
G^4_{24}	0.6	3.6
G^4_{90}	0.5	1.2
G^2_{60}	0.3	0.5
G^4_{94}	0.3	1.7

cance, and these are included along with the previous operators in column GW of the table. RMS errors are lowered once again, but could still be improved. Also note that the $\mathrm{g}_{iq}^{(k)}$ and $\mathrm{w}^{(SL)JM}$ operators are not completely orthogonal since some $\mathrm{g}_{iq}^{(k)}$ values change between the G and GW columns. Such operator non-orthogonality has been a frequently encountered problem in fitting to experimental data where addition of a new operator often significantly alters the existing parameters [19]. For instance, changes in the B_q^k parameters across table 1.6 are due to a slight non-orthogonality of the $\mathrm{C}_q^{(k)}$ and $\mathrm{g}_{iq}^{(k)}$ operators when, as here, the fitting is restricted to the matrix upper diagonal.

A graphical representation of what is happening is shown in figures 1.18 through 1.21. The first figure shows the 91-square canonical EBS model Hamiltonian in the chosen state ordering convention. Each dot represents a non-zero matrix element and all allowed elements are filled, *i.e.* the blanks in this picture are all non-allowed elements. The state ordering scheme is of descending M value, *viz.*

$$|1\,5\,6\,6\rangle, |0\,6\,6\,6\rangle, |1\,5\,5\,5\rangle, \ldots\ |0\,6\,6\text{-}5\rangle, |0\,5\,6\text{-}6\rangle, |0\,6\,6\text{-}6\rangle$$

With this arrangement the allowed states are divided into isolated bands by q label. Bestrewn along the main diagonal are $q = 0$ states, to either side are $q = 4$ then $q = 8$ bands, and in each of the top-right and bottom-left corners are four $q = 12$ configurations. Any other values of q are prevented by the S_4 ($\sim D_{2d}$) site symmetry, just as k is required to be even.

Figures 1.19, 1.20 and 1.21 depict the various CFE fits to this Hamiltonian. Each matrix element of a given operator connects a pair of two-electron states, $\langle 1|\mathrm{Q}|2\rangle$, from the Russell-Saunders basis. There is an angular momentum difference between these two states of $|M_1 - M_2|$. This number defines the minimum allowed operator k (as in $\mathrm{C}_q^{(k)}$) value and q may not exceed k.

The first eight free-ion operators from table 1.6, $\mathrm{E}_{\mathrm{AVG}}$, the Slater operators and α, β, γ are angular momentum scalars and so only connect $|SLJM\rangle$ defined states with themselves, all state labels being angular momentum terms. Consequently these operators are all diagonal matrices, which clearly cannot describe $q \neq 0$ bands. The spin-orbit coupling, Marvin and magnetic operators are non-diagonal but are still restricted to the $q = 0$ central band. The CF operators proper, as defined in equation (1.1), are restricted to $k \leq 6$ since the maximum one-electron angular momentum M for an $|SLJM\rangle$ state is ± 3. This allows $q \in 0, 4$ as seen in table 1.6 and figure 1.19 where it is apparent that CF operators describe low q bands, but not $q \in 8, 12$.

Figure 1.18: $4f^2$ model of EBS matrix

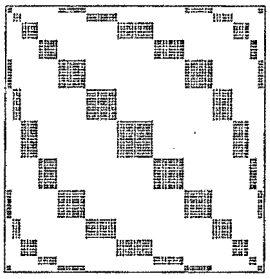

Figure 1.19: CF, δ and $\delta(6)$ Hamiltonians

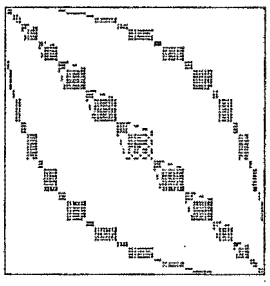

Figure 1.20: G fitted Hamiltonian

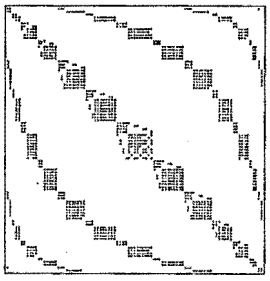

Figure 1.21: GW fitted Hamiltonian

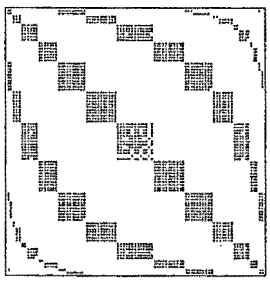

Going to the usual δ CCF, or even $\delta(6)$ CCF, definitely improves the numbers within the filled elements of this picture since the RMS errors are lessened, but there are no new filled elements since obviously $k \leq 6$ and therefore $q \leq 4$. The CF, δ CCF and $\delta(6)$ CCF plots all look exactly the same, no new angular-momentum transitions are being modeled.

With a generalised set of $g_{iq}^{(k)}$ operators, k can suddenly take any integer value, although odd k $g_{iq}^{(k)}$'s are orthogonal to the Hamiltonian and return a parameter of zero as suggested by the symmetry requirements mentioned above. Fitting these operators produces figure 1.20 where suddenly $q \in 8, 12$ bands are considered. Noticeably, no new $q \in 0, 4$ elements are filled because, like the CF operators beforehand, all the $g_{iq}^{(k)}$'s are spin-independent.

To plug some of the gaps then, it is sensible to introduce operators describing spin-dependent interactions; the $w^{(SL)JM}$'s. Sure enough these fill most of the missing elements as shown in figure 1.21, but only within the $q \in 0, 4$ bands once more. For these operators, q is identified with M, and from table 1.6 there are only $M = 0$ and $M = 4$ terms present amongst the thirteen W^{SLJM}parameters.

Further Improving the match behoves an appeal to two-electron spin-dependent CCF operators $(w^{(S_1L_1)}w^{(S_2L_2)})^{(SL)JM}$. For these, S_1 and L_1 are coupled to form J_1, which with J_2 gives S and L which give J then M. In fact the entire CCF parametrisation can be made with these coupled-W operators since spin-independent operators, for instance, can be recovered by putting $S_1 = S_2 = 0$. The operators are required by symmetry to be time-even, and are formed by coupling together pairs of HT-even or HT-odd (but not even with odd) $w^{(SL)J}$ operators as determined from table 1.8, reproduced from [41].

Table 1.8: Fermion one-body operators $w^{(S,L)J}$ (from [41])

HT-odd	$w^{(1,0)1}$	$w^{(0,1)1}$	$w^{(0.3)3}$	$w^{(0,5)5}$
	$w^{(1,2)1,2,3}$	$w^{(1,4)3,4,5}$	$w^{(1,6)5,6,7}$	
HT-even		$w^{(0,2)2}$	$w^{(0,4)4}$	$w^{(0,6)6}$
	$w^{(1,1)0,1,2}$	$w^{(1,3)2,3,4}$	$w^{(1,5)4,5,6}$	

This results in over two thousand non-orthogonal operators, with only 1087 allowed upper diagonal matrix elements for fitting to, causing the non-unique parameter solutions outlined before. Worse still, if the model EBS matrix is block diagonalised, one state from each of the 21 pairs of degenerate states goes into one

block, and the other into another. The result is two identical blocks within the EBS model and so the number of independent, free matrix elements is reduced from 1087 to 856 by the number of elements in the upper diagonal of a 21-square block. (There are no non-allowed states in these blocks, they are all 'solid' matrices.)

What to do with the over-complete set of operators? The solution adopted here is of the same spirit as that adopted by others in similar situations [19, 32]. All operators encountered here, from CF onwards, are placed in the order in which they have been encountered. The matrices are turned into vectors simply by unstacking the rows, and orthogonalised top-to-bottom by the Gram-Schmitt procedure. (Actually, only the allowed upper-diagonal elements are used.) At the end of this, only 763 operators remain. The physical interpretation of these is unclear but many of the non-orthogonal operators mentioned so far are a bit hazy anyway.

These 763 span the space of allowed matrix elements and so fit the canonical EBS model with (orthogonalised) CCF operators exactly. Although conceptually simple, restoring parameters for the original 763 unorthogonalised operators is computationally impractical since in running the Gram-Schmidt procedure backwards there are 2^{N-n} terms which must be identified and summed to return the nth original operator's parameter from a set of N orthogonal operator parameters.

But recall that there are only 856 independent data points. Starting with some large set of random number operators and orthogonalising these would result in a set exactly fitting the EBS model and with at most 856 elements in it. The difference between this number and 763 is so small as makes no odds, and certainly there is no case for pointing to a few predominant physical effects to turn into CCF operators and explain away the EBS matrix. In any case, the worth of a 763 parameter theory is rather questionable.

Lastly, figure 1.22 is a histogram of the number of orthogonal operators within each indicated magnitude range. Magnitude is defined similarly to before, taking the maximum absolute value of parameter times element over the entire operator upper diagonal rather than just the $^1D_2$ multiplet, but now the base ten logarithm of this is taken as well. The distribution is more or less normal, with the most significant operators as named being those that have been historically favoured. Of course, these were also near the top end of the orthogonalisation list and so have had lesser amounts thrown away than have the latter operators. RMS errors from fitting all operators of each magnitude and above are given below in table 1.9. Zero operators refers to the RMS matrix element of the model EBS Hamiltonian itself.

Figure 1.22: Orthogonal operator magnitudes

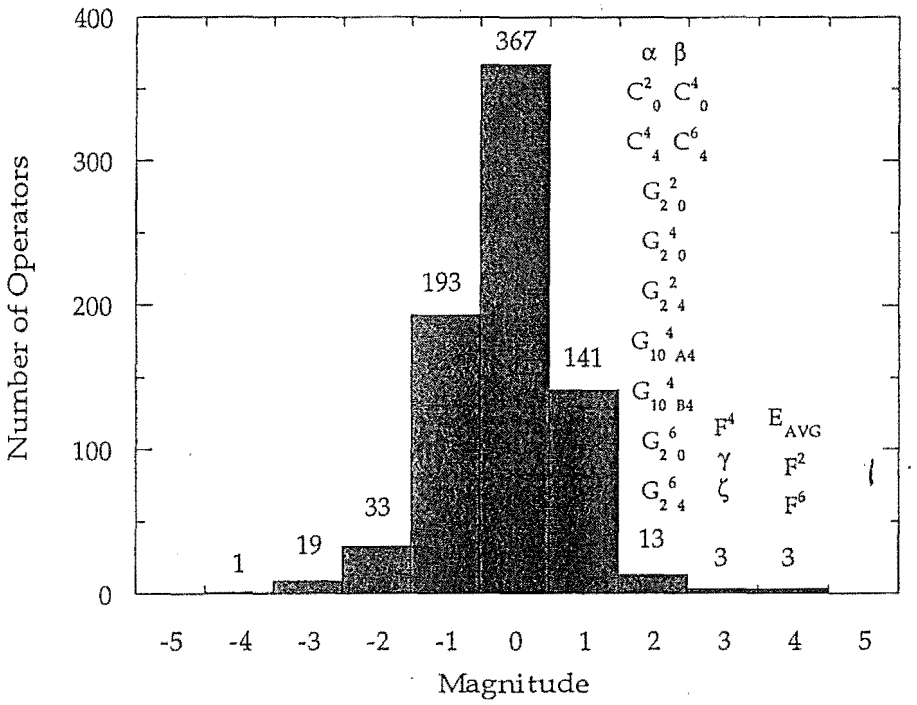

Table 1.9: Effect of additional operators

Operators	RMS σ(H)
0	3866
3	818
6	155
19	29
160	10
527	0.82
720	0.031
753	2×10^{-3}
762	1×10^{-5}
763	8×10^{-12}

It is important to note that the histogram and table were generated using a different full EBS Hamiltonian than has been in use previously. These results were obtained before the others of this section, and the Hamiltonian suffered from some of the $F^0(fp) - F^0(ff)$ estimation problems mentioned. The calculation is extremely time consuming and there has been no opportunity, or wish for that matter, to repeat it. Although the details may differ, the overall behaviour should remain the same and it is this which is important here. In essence, although a small number of more important operators account for the bulk of the observed energies and make the most impact on RMS error, there are a large number of individually small to medium operators the combined effect of which is by no means negligible.

Returning to tables 1.2, 1.3 and 1.4, as far as free-ion and CF parameters are concerned, regardless of the initial EBS parameter value, the CFE value for fitting CCF operators to the model EBS Hamiltonian turns out approximately the same as the CCF parameter from fitting to experimental data. This makes sense in light of the fact that both EBS and CCF operator sets contain these free-ion and crystal field terms. Although the original EBS and CCF operators must differ due to the disparate basis sets, the *model* EBS operators should approximately match the CCF operators provided the reduction procedure is valid and that both correlation and configuration perturbations of the CF Hamiltonian are small. Hence the $4f^2$ component of free-ion and crystal field EBS parameter-times-operator should be roughly the same as the CCF term, and the CFE value of fitting CCF to model EBS ought to be more or less the same as the CCF value. But there are no EBS equivalents to the CCF $\mathrm{g}_{iq}^{(k)}$ operators and therefore no such terms in the $4f^2$ model. As a result there is no clear relation between CFE and CCF G_{iq}^k parameters, with several very large differences appearing in the tables. Notably the delta-function ratios of the CCF parameters are not translated into the G_{iq}^k ratios of the CFE fit.

1.7 Conclusions

A method has been presented which enables a Hamiltonian to be reduced to a form describing a subset of its original eigenstates without changing the basis upon which that subset is defined. This technique was subsequently applied to three configuration interaction (extended basis set) Hamiltonians, producing model Hamiltonians describing only the $4f^2$ states common to both the configuration interaction and correlation crystal field formulations. Fitting crystal field operators to this model showed the free ion and crystal field effects included in both formulations to be highly similar.

Correlation operator parameters obtained by fitting to the model differed more significantly from those resulting from fitting to experimental data. Discrepancies were as large as a factor of ten, although two or three was more typical and there are still some similarities between the parameter sets. The difference here can be attributed to the absence of two-body correlation operators in the original configuration Hamiltonian.

An exact reproduction of the model (single-body spin-independent) configuration Hamiltonian was only achieved by use of orthogonalised general two-body spin-dependent correlation operators. The number of operators required was not appreciably different from the number of matrix elements in the model Hamiltonian, and the reproduction is simply due to the space spanning properties of this set of correlation operators rather than to any particular small set of physical interactions.

Chapter 2

Polarised Transition Interference

Good artists copy, great artists steal. – *Picasso*

2.1 Introduction

The preceding chapter's crystal field theory is concerned with the location of spectral lines but says nothing of their relative intensity. Rest assured that intensity theory is equally well developed [3, 33, 34], indeed it takes on a similar parameters times operators form, and yet the present chapter shall be devoid of the topic. Rather, the subject treated here is of polarisation dependent *interference* between intensities along different axes [7, 8, 38].

The interference in question is a site symmetry dependent phenomenon of optically excited ions embedded within a crystal host. In sites of D_2 or higher symmetry just three measurements, one along each Cartesian axis, are sufficient to reproduce the intensity in any direction since the x, y and z direction dipole moment components transform independently under rotations and do not interfere. In fact, for very high symmetries less than three measurements are required; uniaxial symmetric sites need but two, π (z axis) and σ (x-y plane), whilst octahedral sites would need only one. But for low symmetry sites like C_1, C_2 and C_s, the Cartesian components of the dipole moment operator have more complex transformation properties and may interfere with one another. This necessitates taking more than three measurements as given by table 2.1, the fourth and higher being at some oblique angle to the Cartesian axes.

For a completely general transition from initial state $|i\rangle$ to final state $|f\rangle$ with polarisation vector $\mathbf{E}$ of the emitted or absorbed photon, the transition intensity would be expected to have the form

$$|D_x \cos\theta_x + D_y \cos\theta_y + D_z \cos\theta_z|^2 \tag{2.1}$$

where θ_x is the angle between $\mathbf{E}$ and the x axis (see figure 2.1), and D_x means the matrix element of the dipole moment operator $\mathbf{D}_x$ *viz.* $\langle f|\mathbf{D}_x|i\rangle$. These (in

general complex valued) elements are transition amplitudes, with corresponding transition intensities being absolute amplitudes squared. Expansion of this equation reveals cross terms with the form $D_x^* D_y \cos\theta_x \cos\theta_y$ *etc*, which represent interference between transition amplitudes along the different axes.

But there is no interference between terms belonging to axes which transform as different irreducible representations ("irreps") of the transition centre's point group, *i.e.* in D_2 or higher symmetries where each of the x, y and z directions are independent (see figure 2.2), nor in uniaxial symmetry where x and y are two distinct basis functions of a common two-dimensional irrep. For such cases, the cross terms in equation (2.1) should cancel out, say D_x will be real and D_y pure imaginary for instance, and the intensity simplifies to equation (2.2).

$$|D_x|^2 \cos^2\theta_x + |D_y|^2 \cos^2\theta_y + |D_z|^2 \cos^2\theta_z \tag{2.2}$$

No such cancellation occurs for low symmetry point groups, an example of which is C_s having only the identity and a single mirror plane as symmetry operations [1, 29]. This causes the three Cartesian basis vectors x, y, z to transform with only two single-dimensional irreps γ_1 and γ_2. By convention, the z axis is taken as independent of the others, transforming as γ_2, leaving x and y to transform together under the first irrep γ_1. With this choice of association, the x and y directions define the C_s mirror plane and z, being perpendicular to this plane, is the C_s axis. This distinction between the x-y plane and the z axis makes cylindrical coordinates more convenient, and the transition intensity $|D_\phi|^2$ at an arbitrary direction angle $\phi \in [0 : \pi/2]$ from x towards y (*i.e.* in the x-y plane, figure 2.1), is given by

$$\begin{aligned} |D_\phi|^2 &= |D_x \cos\phi + D_y \sin\phi|^2 \\ &= |D_x|^2 \cos^2\phi + (D_x^* D_y + D_y^* D_x)\cos\phi\sin\phi + |D_y|^2 \sin^2\phi \end{aligned} \tag{2.3}$$

The high symmetry non-interfering approximation to this equation would be

$$|D_\phi|^2_{\mathrm{HS}} \approx |D_x|^2 \cos^2\phi + |D_y|^2 \sin^2\phi \tag{2.4}$$

Being associated with a second irrep, the z direction amplitude does not interfere with either D_x or D_y, *i.e* the high symmetry approach is valid for the z component. Taking as an example a direction given by some angle $\theta \in [0 : \pi/2]$ from z towards x in the x-z plane, the complex nature of the amplitudes comes to the fore, and cross terms cancel to aught leaving

$$\begin{aligned} |D_\theta|^2 &= |D_x \sin\theta + D_z \cos\theta|^2 \\ &= |D_x|^2 \sin^2\phi + |D_z|^2 \cos^2\phi \end{aligned} \tag{2.5}$$

Now high symmetry (non-interfering) approximations such as equation (2.2) have been in use within the field for some time and there has seemingly been no endeavor to look for interference effects in the laboratory. Numerical modeling of hypothetical high symmetry (D_2 and C_{4v}) crystal centres did indeed show equations (2.1) and (2.2) to produce identical results. Somewhat more importantly, a treatment of hypothetical C_s symmetric data justified the expectation that although (2.2) and (2.4) break down for C_s symmetry, the generalised form of (2.1), (2.3) and (2.5) still holds.

This theory of low symmetry polarised interference first appeared in [38] where it was noted that

> It would be interesting to check this result experimentally, although, as with many effects discussed in this paper requiring a thorough study of geometrical dependence, experimental complications would be a significant challenge, particularly in low-symmetry systems where non-equivalent sites may be common.

and here the eventual aim is to suggest a particular transition suitable for experimental tests of interference phenomena. This deals specifically with hydrogenated CaF_2:Pr^{3+}, but the analysis is equally applicable to any other C_s site-symmetric rare-earth^{3+} centre embedded within a cubic lattice. Drawing heavily upon [27] and [28], sections 2.2 and 2.3 describe the nature of C_s symmetric hydrogenated CaF_2:Pr^{3+} sites and their polarisation dependent transition intensities along the Cartesian axes. Section 2.4 makes interference predictions for other directions and suggests candidate transitions with which the effect might possibly be seen. In section 2.5, some practical considerations are addressed with the conclusion that although there do indeed exist randomly oriented non-equivalent sites, their combined effect should still exhibit the interference phenomena sought after. Lastly section 2.6 summarises the results and identifies candidate transitions in terms of Pr^{3+} ion states.

Table 2.1: Intensity measurements by point group (summarised from [38]). To illustrate this table, the group O has a single three-dimensional irrep and only one measurement is required to characterise the (isotropic, polarisation independent) emission intensity. The group C_∞ has a one-dimensional irrep, a second one-dimensional irrep and the conjugate of this irrep. Two measurements are required, one along the z axis (axial π direction) and another in the x-y plane (perpendicular σ direction). The group C_1 has three identical one-dimensional irreps requiring six measurements, one along each axis plus another in each plane.

Irrep Dimensions	Crystallographic Point Groups	Required Measurements
3	O O_h K K_h T T_h T_d	1 (any)
$1 \oplus 2$	D_∞ $C_{\infty v}$ D_6 C_{6v} D_{3h} D_{6h} D_5 C_{5v} D_{5d} D_4 D_{2d} C_{4v} D_{4h} D_3 C_{3v} D_{3d}	2 (x-y, z)
$1 \oplus (1 \oplus 1^*)$	C_∞ $C_{\infty h}$ C_6 C_{3h} C_{6h} C_5 C_{5i} C_4 S_4 C_{4h} C_3 C_{3i}	2 (x-y, z)
$1 \oplus 1 \oplus 1$	D_2 C_{2v} D_{2h}	3 (x, y, z)
$1 \oplus 1^2$	C_2 C_s C_{2h}	4 (x, y, x-y, z)
1^3	C_1 C_i	6 (x, x-y, y; z-x, z, y-z)

Figure 2.1: Angular coordinate systems. On the left, a direct axis-to-vector system where three angles $\in [0, \pi]$ are required to specify the direction of $\mathbf{E}$, and on the right, the conventional altitude-azimuth system where projection of $\mathbf{E}$ into the x-y plane enables a choice of cyclic direction for $\phi \in [0, 2\pi]$, dispensing with one angular coordinate.

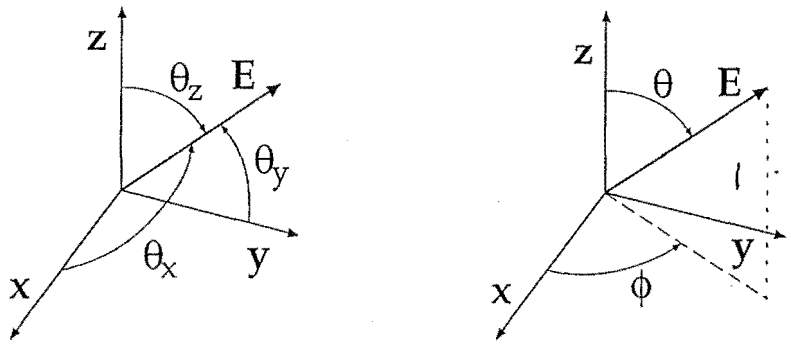

Figure 2.2: Cartesian axis irreps. On the left a high symmetry centre where all axes transform as different irreps, and low symmetry on the right, where x and y transform with the same irrep.

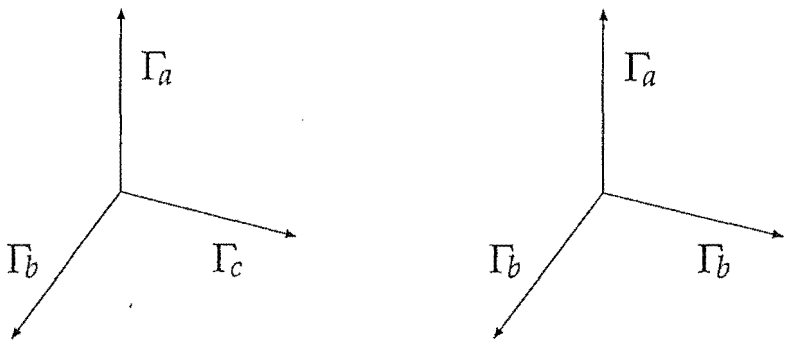

2.2 Praseodymium C_s Centres

Arbitrary high symmetry (*e.g.* D_2, C_{4v}) centres do not exhibit interference between the polarisations of different Cartesian axes which all transform as disparate basis functions of the point group's irreps. Low symmetry centres on the other hand are expected to display this interference and here the general idea is to look for interference between x and y polarisations in C_s symmetries. Numerical treatment of a hypothetical C_s system does indeed show the expected behaviour, with both constructive and destructive interference observed. The magnitude of these effects is often quite large, the difference between equations (2.3) and (2.4) being as much as $\pm 100\%$ of the high symmetry approximation, dependent upon the relative phases of D_x, D_y and D_z (see figure 2.12).

The next obvious step is to find a suitable C_s symmetric compound and hydrogenated CaF_2:Pr^{3+} was chosen. As a rare-earth doped halide it falls into a class of extensively studied, thoroughly characterised materials [20, 27, 28, 31] which have also been the subject of much theoretical analysis [5, 26, 41]. The most pertinent feature regarding polarised interference measurements is that CaF_2 crystals ("fluorite") are cubic structured, the advantage being that cubic crystals are not intrinsically dichroic and polarisation of the incident laser beam is unaffected by the crystal. Without this attribute there would be no way of knowing what polarisation was being seen by target centres within their host material.

A single unit cell of undoped, unhydrogenated, pure CaF_2 is shown in figure 2.3. For clarity the actual sizes of the ions have been reversed, with Ca^{2+} ions appearing as large grey spheres and F^- ions as small white spheres. The overall cubic structure may be regarded as a mesh of primitive cubic latticed fluoride ions and a face centred cubic array of calcium ions [29].

Figure 2.3: Fluorite unit cell (after [29])

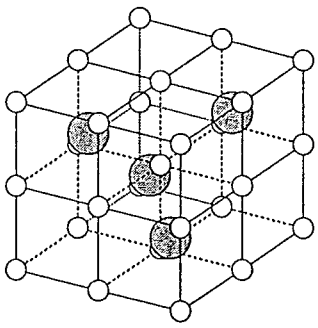

Each calcium ion sits in an octahedral (O_h) site, being immediately surrounded by four fluorides. Whilst edge-adjacent fluoride cells also contain calcium ions, the six face-adjacent cells are vacant. Figure 2.4 shows more clearly a single calcium ion in its O_h site and an empty face-adjacent cell.

Figure 2.4: Calcium ion within fluoride lattice (after [27])

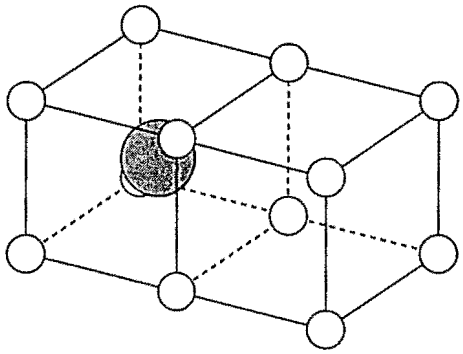

When the crystal is grown with a Pr^{3+}/H^- dopant mixture some of the calcium sites are instead filled with praseodymium ions. To account for the charge difference a vacant face-adjacent site is then occupied by a hydride [27] as shown in figure 2.5. The large black sphere in the figure is the praseodymium ion and the small black sphere the hydride. At low concentrations (typically 0.05 mol% [28]), each Pr^{3+} centre is essentially isolated from all others and the site symmetry is determined purely by the immediately surrounding crystal. This arrangement results in C_{4v} site symmetry for the centre. The Cartesian axes indicated are for the centre coordinate system and other orientations with respect to the crystal axes are of course possible [27, 28].

Now C_{4v} centres are not predicted to show any interference effects, but the fluoride and hydride ions carry equal charge and so hydrides may be freely substituted for fluorides on the primitive cubic lattice. Figures 2.6 and 2.7 depict lower symmetry centres arising from just this exchange. Again centre relative axes are shown and different orientations also exist. The shading in figure 2.6 indicates the C_{2v} plane. Unlike C_s centres, the axial vector perpendicular to the plane is $\mathbf{x}$ and not $\mathbf{z}$.

The symmetry of interest was chosen to be C_s where the z transition moment component does not interfere with the x or y components ($\mathbf{z}$ transforms as the irrep γ_2 whilst $\mathbf{x}$ and $\mathbf{y}$ transform together as γ_1), simplifying the expected interference behaviour into two-dimensions. There are two classes of hydrogenated $CaF_2{:}Pr^{3+}$ C_s centre, namely $C_s(a)$ and $C_s(b)$, each having six possible orientations ("centres"),

Figure 2.5: C_{4v} hydrogenated centre (after [27])

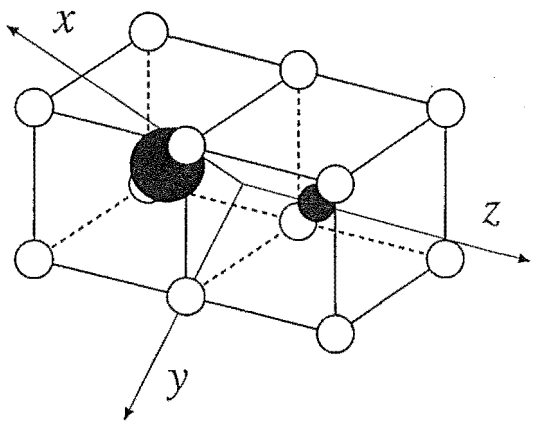

Figure 2.6: C_{2v} hydrogenated centre (after [27])

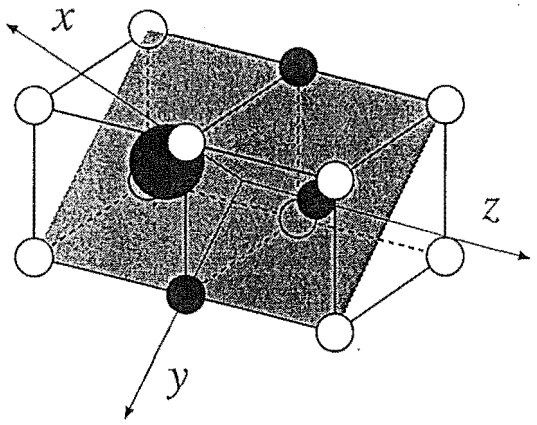

Figure 2.7: C_1 hydrogenated centre (after [27])

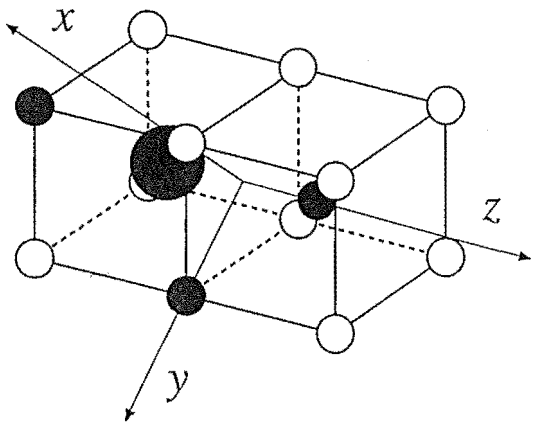

numbered accordingly, within the crystal [21, 28, 27]. All orientations for both types are given in figures 2.9 and 2.10. The centre relative z axis is perpendicular to the shaded C_s (*i.e.* x-y) plane and its orientation in terms of the fixed crystal lattice basis X, Y, Z axes is what distinguishes one centre from another. The classes are defined by the number of fluoride replacing hydride ions; one for $C_s(a)$ and two for $C_s(b)$. More importantly, $C_s(a)$ centre C_s planes are at 45° to the crystal planes whilst $C_s(b)$ centre planes run parallel.

Polarised excitation beams would be directed onto the crystal from along its X axis and any resulting fluorescence recorded along the Z axis (figure 2.8). By translating each centre's own axes relative interference into crystal axes relative effects and measuring the fluorescence intensity for different polarisation directions in the X-Y plane, any deviations from the high symmetry non-interfering equation (2.4) ought to be detectable.

Figure 2.8: Geometrical arrangement of polarisation experiment (after [27])

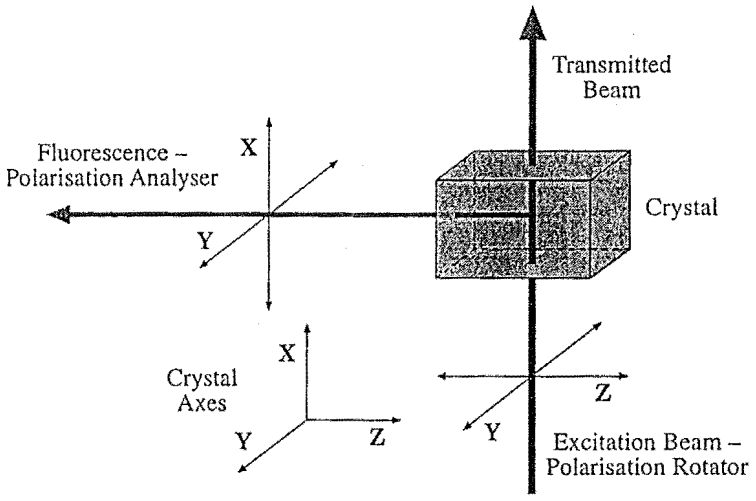

Figure 2.9: $C_s(a)$ centres of hydrogenated CaF_2:Pr^{3+} (after [27]). There are six numbered orientations of the site relative x, y, z axes with respect to the crystal relative X, Y, Z coordinates. The x and y axes of each centre define its shaded C_s plane and the z axis is its C_s site axis.

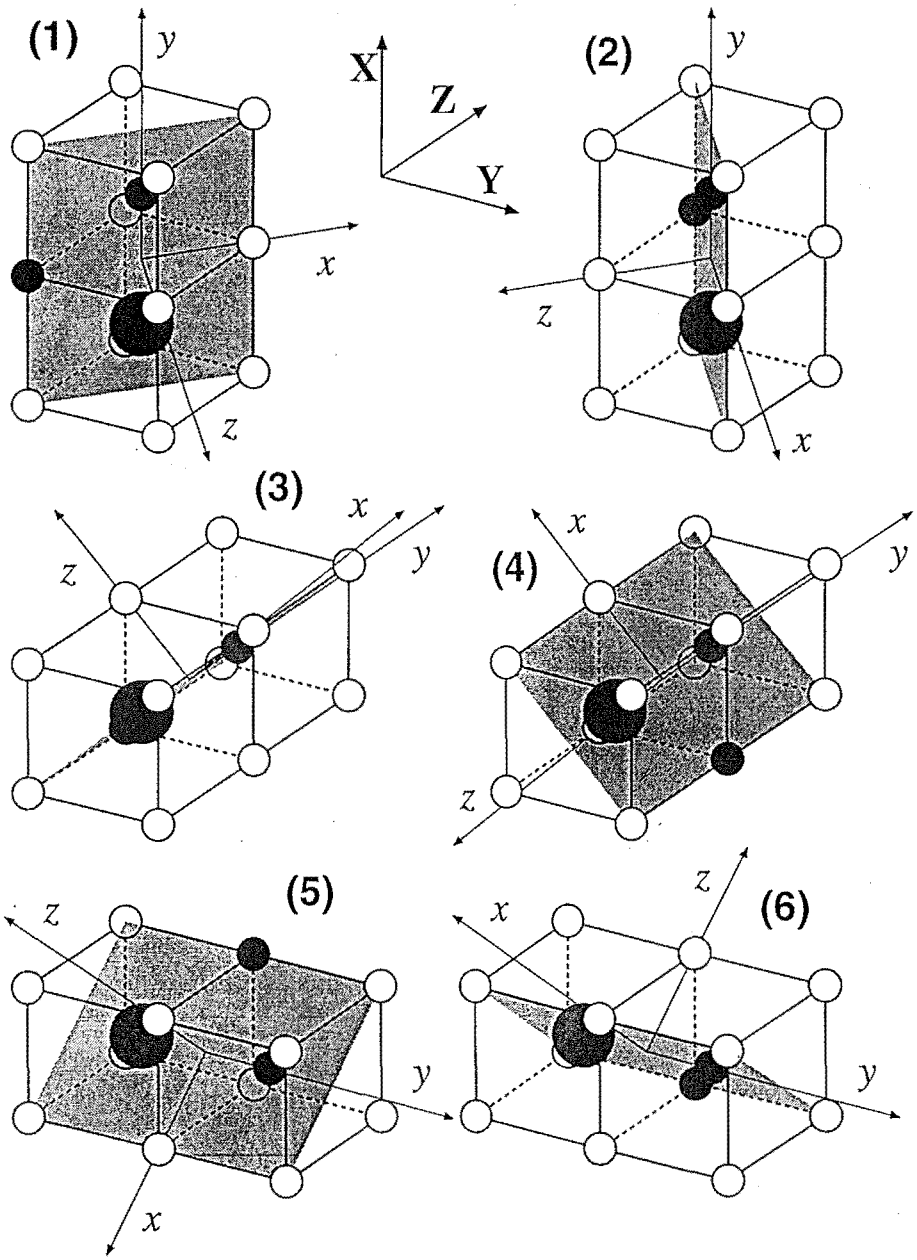

Figure 2.10: $C_s(b)$ centres of hydrogenated CaF_2:Pr^{3+} (after [27]). There are six numbered orientations of the site relative x, y, z axes with respect to the crystal relative X, Y, Z coordinates. The x and y axes of each centre define its shaded C_s plane and the z axis is its C_s site axis.

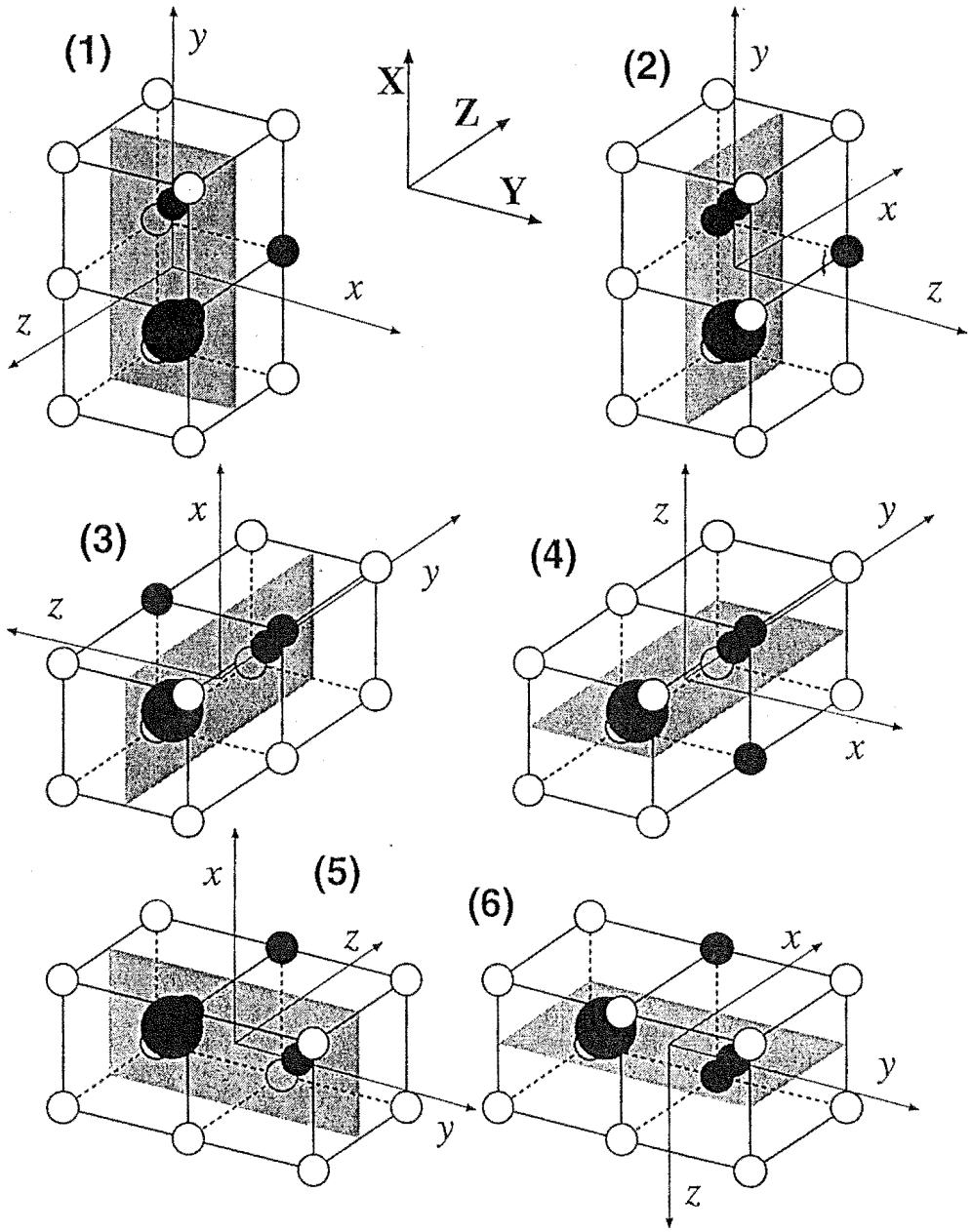

2.3 Polarisation Ratios

For a specific centre, each electric-dipole (E1) allowed transition is associated with a transition moment which may be described in terms of the centre's coordinate axes [27]. In an excitation the moment vector's site centre relative local x, y, z axis components are arbitrarily labelled A, B, C, and D, E, F is adopted for fluorescence. Excitation is the absorption of a photon by a low energy $4f^2$ electron, and fluorescence the subsequent emission. The polarisation direction of a particular transition is also specified in the centre coordinate system via the symmetry axes. Polarisation ratios are defined on the crystal X, Y, Z axes and are summed over all centre orientations.

Tables 2.3 and 2.4 consider all E1-transition possibilities for the two C_s sites. These are reproduced from [27], only this source is in lower case which will be used here for complex valued amplitudes and upper case is substituted in these tables of real valued intensities. Intensity A is related to amplitude a by $A = |a|^2$. Symmetries (irreps) specified for absorption and emission are of the transition polarisaton vectors themselves rather than the terminating states.

The crystal field levels of C_s site-symmetric non-Kramers rare-earth^{3+} ions, such as Pr^{3+} in hydrogenated CaF_2, transform as one of the C_s point group's two single dimensional irreps; γ_1 and γ_2. As indicated in table 2.2, reproduced from an unlabelled table in [28], if the initial and final states behave according to the same irrep, then the transition between them goes by γ_1, otherwise as γ_2. A related diagram of the physical process is given in figure 2.11. For example, if the initial state during an excitation has transformation property $\gamma_a = \gamma_2$ and the final state has $\gamma_b = \gamma_1$, then the transition from one to the other transforms as $\gamma_e = \gamma_2$.

Table 2.2: C_s transition irreps (from [28])

C_s	γ_1	γ_2
γ_1	γ_1	γ_2
γ_2	γ_2	γ_1

Any γ_1 transitions may be σ_x or σ_y (*i.e.* x or y) polarised, the electric-field vector being perpendicular to the site C_s (*i.e.* z) axis. The γ_2 transitions are the opposite; π (*i.e.* z) polarised with the electric-field being along the C_s axis direction. Since the laser excitation beam is taken as incident from the X direction, it may be either

Y or Z (electrically) polarised. Fluorescent emission is detected in the Z direction, allowing X or Y polarisations (see figure 2.8). Emission intensities can be measured for each of these polarisations and the expected ratios have been tabulated in 2.3 and 2.4. For Z polarised excitation, fluorescence polarisation ratios are always 1:1 since fluorescence is measured in the X-Y plane which is symmetrical about the Z axis by virtue of the C_s symmetry. For γ_1 absorption and emission, the polarisation ratios are unrestricted in the range 0:1 to 1:0. Other ratios are constrained by the requirement that all transition moments be positive and real.

The intensities of tables 2.3 and 2.4 can now be transcribed into amplitudes and used to predict where and how much interference should be seen under each possible transition.

Figure 2.11: Physical mechanism of emission–fluorescence process. Labels a, b, c, d may take values from $\{1, 2\}$, and then e, f are given by table 2.2. The letters in this figure are unrelated to those of tables 2.5 and 2.6.

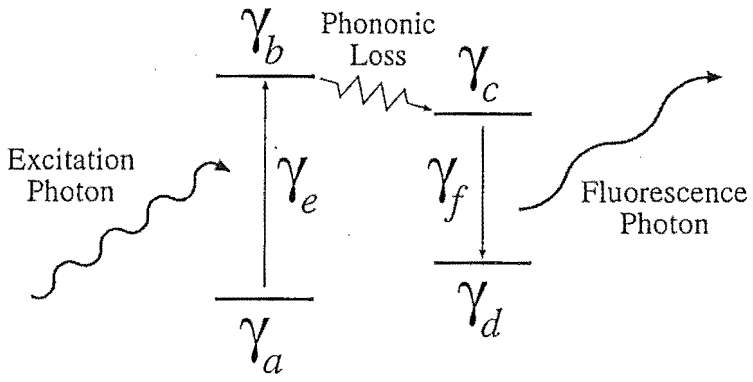

Table 2.3: E1-transition polarisation ratios for the symmetry $C_s(a)$ (from [27])

Excitation	Fluorescence		Centre (1)	(2)	(3)	(4)	(5)	(6)	Ratio X : Y
γ_1 Y			$\frac{1}{2}A$	$\frac{1}{2}A$	$\frac{1}{2}A$	$\frac{1}{2}A$	B	B	
	γ_1	X	$\frac{1}{2}AE$	$\frac{1}{2}AE$	$\frac{1}{4}AD$	$\frac{1}{4}AD$	$\frac{1}{2}BD$	$\frac{1}{2}BD$	$\frac{1}{2}AD + BD + AE$
		Y	$\frac{1}{4}AD$	$\frac{1}{4}AD$	$\frac{1}{4}AD$	$\frac{1}{4}AD$	BE	BE	$: AD + 2BE$
	γ_2	X	0	0	$\frac{1}{4}AF$	$\frac{1}{4}AF$	$\frac{1}{2}BF$	$\frac{1}{2}BF$	
		Y	$\frac{1}{4}AF$	$\frac{1}{4}AF$	$\frac{1}{4}AF$	$\frac{1}{4}AF$	0	0	$\frac{1}{2}A + B : A$
Z			$\frac{1}{2}A$	$\frac{1}{2}A$	B	B	$\frac{1}{2}A$	$\frac{1}{2}A$	
	γ_1	X	$\frac{1}{2}AE$	$\frac{1}{2}AE$	$\frac{1}{2}BD$	$\frac{1}{2}BD$	$\frac{1}{4}AD$	$\frac{1}{4}AD$	
		Y	$\frac{1}{4}AD$	$\frac{1}{4}AD$	$\frac{1}{2}BD$	$\frac{1}{2}BD$	$\frac{1}{2}AE$	$\frac{1}{2}AE$	1 : 1
	γ_2	X	0	0	$\frac{1}{2}BF$	$\frac{1}{2}BF$	$\frac{1}{4}AF$	$\frac{1}{4}AF$	
		Y	$\frac{1}{4}AF$	$\frac{1}{4}AF$	$\frac{1}{2}BF$	$\frac{1}{2}BF$	0	0	1 : 1
γ_2 Y			$\frac{1}{2}C$	$\frac{1}{2}C$	$\frac{1}{2}C$	$\frac{1}{2}C$	0	0	
	γ_1	X	$\frac{1}{2}CE$	$\frac{1}{2}CE$	$\frac{1}{4}CD$	$\frac{1}{4}CD$	0	0	
		Y	$\frac{1}{4}CD$	$\frac{1}{4}CD$	$\frac{1}{4}CD$	$\frac{1}{4}CD$	0	0	$\frac{1}{2}D + E : D$
	γ_2	X	0	0	$\frac{1}{4}CF$	$\frac{1}{4}CF$	0	0	
		Y	$\frac{1}{4}CF$	$\frac{1}{4}CF$	$\frac{1}{4}CF$	$\frac{1}{4}CF$	0	0	1 : 2
Z			$\frac{1}{2}C$	$\frac{1}{2}C$	0	0	$\frac{1}{2}C$	$\frac{1}{2}C$	
	γ_1	X	$\frac{1}{2}CE$	$\frac{1}{2}CE$	0	0	$\frac{1}{4}CD$	$\frac{1}{4}CD$	
		Y	$\frac{1}{4}CD$	$\frac{1}{4}CD$	0	0	$\frac{1}{2}CE$	$\frac{1}{2}CE$	1 : 1
	γ_2	X	0	0	0	0	$\frac{1}{4}CF$	$\frac{1}{4}CF$	
		Y	$\frac{1}{4}CF$	$\frac{1}{4}CF$	0	0	0	0	1 : 1

Table 2.4: E1-transition polarisation ratios for the symmetry $C_s(b)$ (from [27])

Excitation		Fluorescence		Centre						Ratio X : Y
				(1)	(2)	(3)	(4)	(5)	(6)	
γ_1	Y			A	0	0	A	B	B	
		γ_1	X	AE	0	0	0	BD	0	$AE+BD$:
			Y	AD	0	0	AD	BE	BE	$\|2AD+2BE$
		γ_2	X	0	0	0	AF	0	BF	
			Y	0	0	0	0	0	0	1 : 0
	Z			0	A	B	B	0	A	
		γ_1	X	0	AE	BD	0	0	0	
			Y	0	0	0	BD	0	AE	1 : 1
		γ_2	X	0	0	0	BF	0	AF	
			Y	0	AF	BF	0	0	0	1 : 1
γ_2	Y			0	C	C	0	0	0	
		γ_1	X	0	CE	CD	0	0	0	
			Y	0	0	0	0	0	0	1 : 0
		γ_2	X	0	0	0	0	0	0	
			Y	0	CF	CF	0	0	0	0 : 1
	Z			C	0	0	0	C	0	
		γ_1	X	CE	0	0	0	CD	0	
			Y	CD	0	0	0	CE	0	1 : 1
		γ_2	X	0	0	0	0	0	0	
			Y	0	0	0	0	0	0	0 : 0

2.4 Interference Effects

Presented in tables 2.5 and 2.6 are the expected interference phenomena for each centre and absorption-emission orientation. Each intensity A, B, C, D, E, F is associated with some transition moment amplitude a, b, c, d, e, f such that $|a|^2 = A$, $|b|^2 = B$ *etc.* All terms in these two tables are taken to be followed with the ubiquitous $\cos\phi \sin\phi$ angular dependence factor from equation (2.3) and are obtained by substituting lower for upper case (amplitudes for intensities, square-rooting any numerical values) in tables 2.3 and 2.4, then evaluating the difference between equation (2.3) and high symmetry (cross-term deficient) approximation. In other words, the expressions appearing in these two tables are just the cross-terms of equation (2.3). Although defined in terms of complex amplitudes, the terms appearing in these tables all mix complex numbers with their conjugates and are in fact real intensities. They can however be negative, it is only the total intensity (sum of all terms) in equation (2.3) which must be positive. In the transitions column, $\gamma_1(Y)\gamma_2$ means absorption of Y polarised light via a γ_1 transition, followed by fluorescence from a γ_2 emission. The emission polarisation vector lies in the crystal relative X-Y plane, its direction being defined by the angle ϕ as per figure 2.1.

For purposes of seeing such interference effects, the simplest cases to consider would be $C_s(b)$ sites with either Y polarised γ_1 or Z polarised γ_2 absorption, and then a γ_1 emission. Interference should be seen in a rotation from **X** to **Y** in the emission polarisation. Besides these two $C_s(b)$ sites there are several $C_s(a)$ candidates, the only non-interference transition being $\gamma_2(Z)\gamma_2$ which involves transitions only between states of different irreps. The bulk of interference behaviour is due to the $(d^*e + e^*d)$ terms which mix emission polarisations of the rare-earth centre x and y axes. Additional terms are present for the $C_s(a)$ centres where the 45° angle between the crystal and C_s planes spreads moment x, y, z components between the X, Y, Z axes.

Ideally transitions with ratios like 1:0 or 0:1 (producing no interference) should be avoided in favour of those having similar intensities for the X and Y axes. When the polarisation ratio is 1:1, the non-interference equation predicts constant intensity in rotating from **X** to **Y**, but with interference a hump or dip should appear in the middle. Constructive interference can produce intensities as large as double that without interference, whilst destructive interference can give zero intensity at 45° to the X axis.

Table 2.5: Interference terms for $C_s(a)$ centres. All terms should be read as being followed with a $\cos\phi\sin\phi$ angular dependence factor for the X-Y plane (see figure 2.1).

Transition	Centre (1,2)	Centre (3,4)	Centre (5,6)	Sum
$\gamma_1(Y)\gamma_1$	$\frac{1}{\sqrt{8}}\|a\|^2(d^*e+e^*d)$	$\frac{1}{2}\|ad\|^2$	$\frac{1}{\sqrt{2}}\|b\|^2(d^*e+e^*d)$	$\sqrt{2}(\frac{1}{2}\|a\|^2+\|b\|^2)(d^*e+e^*d)+\|ad\|^2$
$\gamma_1(Y)\gamma_2$	0	$\frac{1}{2}\|af\|^2$	0	$\|af\|^2$
$\gamma_1(Z)\gamma_1$	$\frac{1}{\sqrt{8}}\|a\|^2(d^*e+e^*d)$	$\|bd\|^2$	$\frac{1}{\sqrt{8}}\|a\|^2(d^*e+e^*d)$	$\sqrt{2}\|a\|^2(d^*e+e^*d)+2\|bd\|^2$
$\gamma_1(Z)\gamma_2$	0	$\|bf\|^2$	0	$2\|bf\|^2$
$\gamma_2(Y)\gamma_1$	$\frac{1}{\sqrt{8}}\|c\|^2(d^*e+e^*d)$	$\frac{1}{2}\|cd\|^2$	0	$\frac{1}{\sqrt{2}}\|c\|^2(d^*e+e^*d)+\|cd\|^2$
$\gamma_2(Y)\gamma_2$	0	$\frac{1}{2}\|cf\|^2$	0	$\|cf\|^2$
$\gamma_2(Z)\gamma_1$	$\frac{1}{\sqrt{8}}\|c\|^2(d^*e+e^*d)$	0	$\frac{1}{\sqrt{8}}\|c\|^2(d^*e+e^*d)$	$\sqrt{2}\|c\|^2(d^*e+e^*d)$
$\gamma_2(Z)\gamma_2$	0	0	0	0

Table 2.6: Interference terms for $C_s(b)$ centres. All terms should be read as being followed with a $\cos\phi\sin\phi$ angular dependence factor for the X-Y plane (see figure 2.1).

Transition	Centre (1)	Centre (2,3,4)	Centre (5)	Centre (6)	Sum
$\gamma_1(Y)\gamma_1$	$\|a\|^2(d^*e+e^*d)$	0	$\|b\|^2(d^*e+e^*d)$	0	$(\|a\|^2+\|b\|^2)(d^*e+e^*d)$
$\gamma_1(Y)\gamma_2$	0	0	0	0	0
$\gamma_1(Z)\gamma_1$	0	0	0	0	0
$\gamma_1(Z)\gamma_2$	0	0	0	0	0
$\gamma_2(Y)\gamma_1$	0	0	0	0	0
$\gamma_2(Y)\gamma_2$	0	0	0	0	0
$\gamma_2(Z)\gamma_1$	$\|c\|^2(d^*e+e^*d)$	0	$\|c\|^2(d^*e+e^*d)$	0	$2\|c\|^2(d^*e+e^*d)$
$\gamma_2(Z)\gamma_2$	0	0	0	0	0

Figure 2.12 shows how the relative interference, summed over all orientations, in the $C_s(b)$ centres varies with amplitude d. The transition depicted is the near ideal $\gamma_2(Z)\gamma_1$ case of table 2.6 with amplitudes c and e fixed at unity. Putting $d = 0$ shows no interference just as for $d = i$, since all this requires is that the interfering cross term $(d^*e + e^*d)$ be zero. More generally, d and e are complex numbers, which can be thought of as vectors in the complex plane, and there will be no interference if the two are mutually perpendicular. The range of interference effects is as stated before; $\pm 100\%$.

Figures 2.13 through 2.28 show interference behaviour for both centres under each of the eight possible transitions and with all amplitudes set to unity. All six centre orientations have been summed over again since there ought to be equal numbers of each within the bulk crystal.

The graphs are arranged in pairs with the upper graph depicting intensity predictions (in arbitrary units) from the high symmetry approximation, non-interfering equation (2.4) and the generalised interference form of (2.3) which is distinguished by the label "+ i". The lower graph plots the percentage difference between the two equations (relative to the non-interfering) against the angle ϕ from crystal axis X towards crystal axis Y.

There are of course different sets of plots for different amplitudes, but with the choice made here it is the $\gamma_1(Y)\gamma_1$ and $\gamma_1(Z)\gamma_1$ transitions which are the most intense. The most ideal transitions to examine would be $\gamma_1(Z)\gamma_1$, $\gamma_1(Z)\gamma_2$ and $\gamma_2(Z)\gamma_1$ where the non-interfering equation (2.5) predicts uniform intensity between **X** and **Y** so that the interference peaks in between. The worst case of course is $\gamma_2(Z)\gamma_2$ (figures 2.27 and 2.28) where there is only a very low intensity for just the $C_s(a)$ center and no interference at all.

All told, the best options for detecting interference would be both centres in a $\gamma_2(Z)\gamma_1$ transition, either centre with a $\gamma_1(Y)\gamma_1$ transition, or a $C_s(a)$ $\gamma_1(Z)\gamma_1$ transition. It is worth stressing that in these cases the effect being sought is not a small one.

Figure 2.12: $C_s(b)$ site $\gamma_2(Z)\gamma_1$ transition interference variation (summed over all centre orientations, see table 2.6). Plotted is the interference cross-term of equation (2.3) as a percentage of the non-interference terms retained in the high symmetry approximation (2.4).

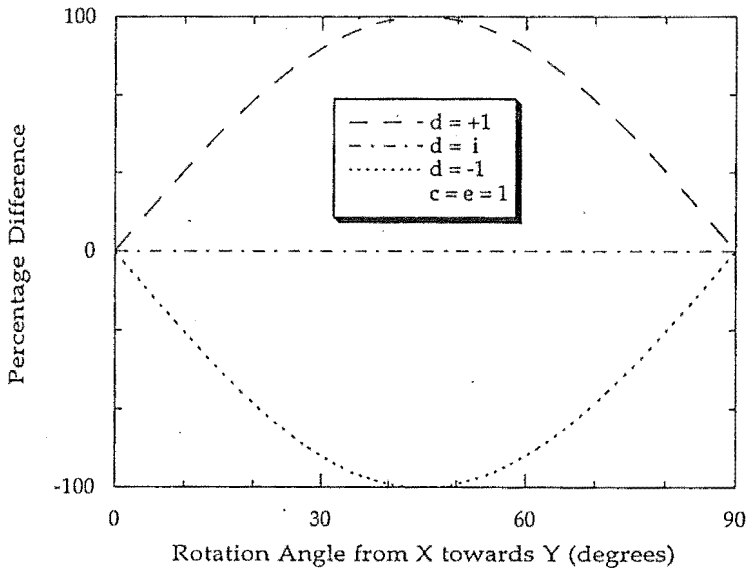

Figure 2.13: $\gamma_1(Y)\gamma_1$ transition interference predictions from the non-interfering equation (2.4) and the generalised interfering form (2.3) denoted by "+ i". Intensities for each site are summed over all centre orientations (tables 2.5, 2.6) with all amplitudes set to unity.

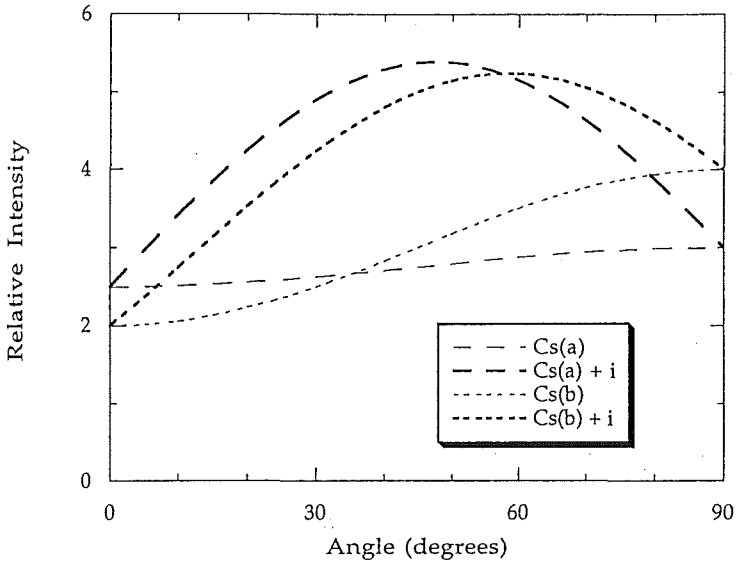

Figure 2.14: $\gamma_1(Y)\gamma_1$ relative interference. Difference between the interfering and non-interfering curves above (cross-term of equation (2.3)), as a percentage of the latter (equation (2.4)).

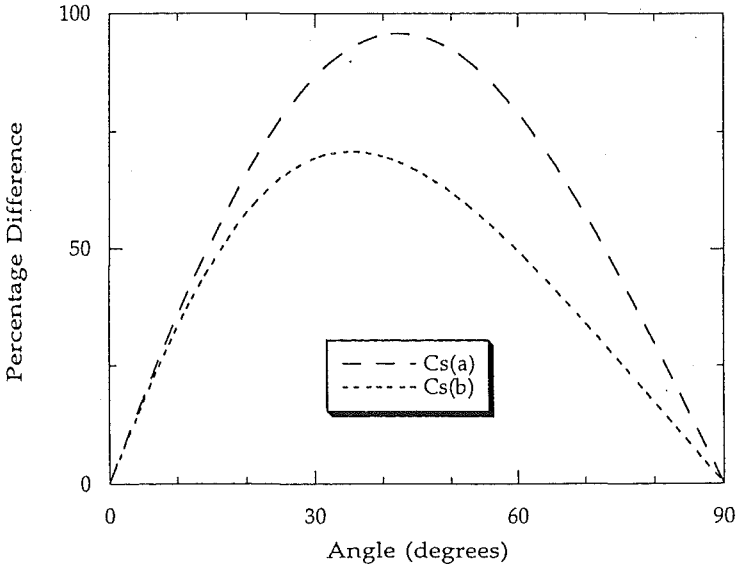

Figure 2.15: $\gamma_1(Y)\gamma_2$ transition interference predictions from the non-interfering equation (2.4) and the generalised interfering form (2.3) denoted by "+ i". Intensities for each site are summed over all centre orientations (tables 2.5, 2.6) with all amplitudes set to unity. There is no interference for the $C_s(b)$ centres.

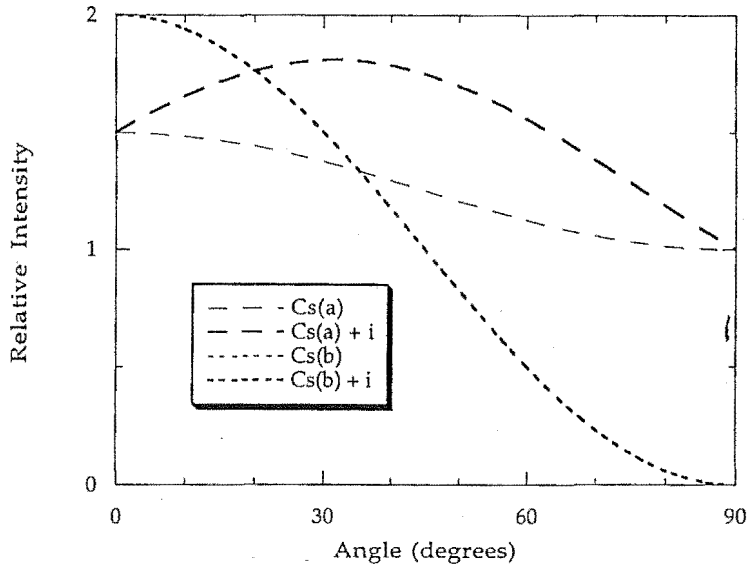

Figure 2.16: $\gamma_1(Y)\gamma_2$ relative interference. Difference between the interfering and non-interfering curves above (cross-term of equation (2.3)), as a percentage of the latter (equation (2.4)).

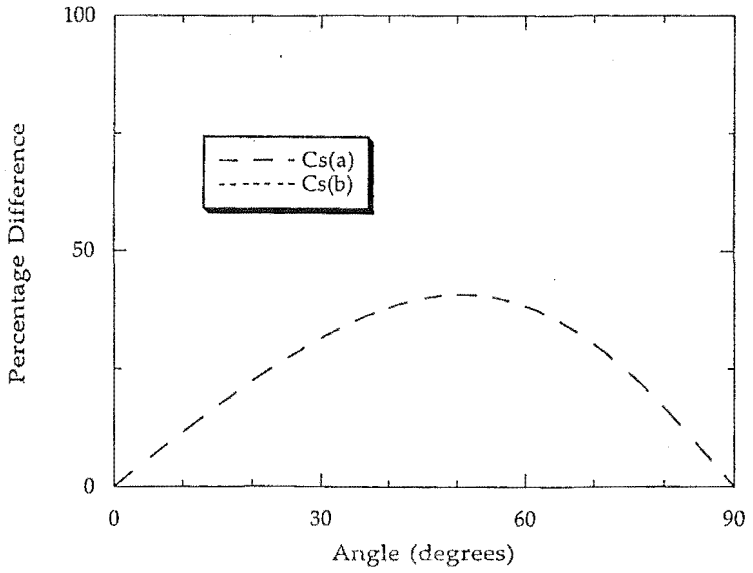

Figure 2.17: $\gamma_1(Z)\gamma_1$ transition interference predictions from the non-interfering equation (2.4) and the generalised interfering form (2.3) denoted by "+ i". Intensities for each site are summed over all centre orientations (tables 2.5, 2.6) with all amplitudes set to unity. There is no interference for the $C_s(b)$ centres.

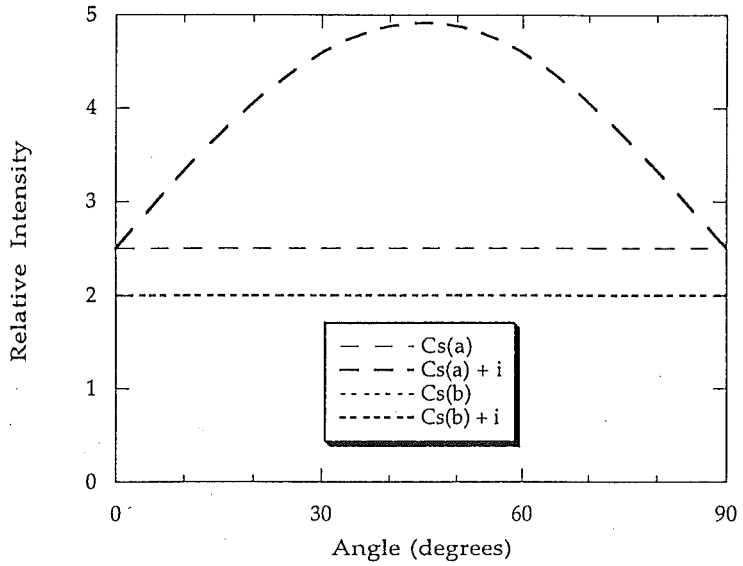

Figure 2.18: $\gamma_1(Z)\gamma_1$ relative interference. Difference between the interfering and non-interfering curves above (cross-term of equation (2.3)), as a percentage of the latter (equation (2.4)).

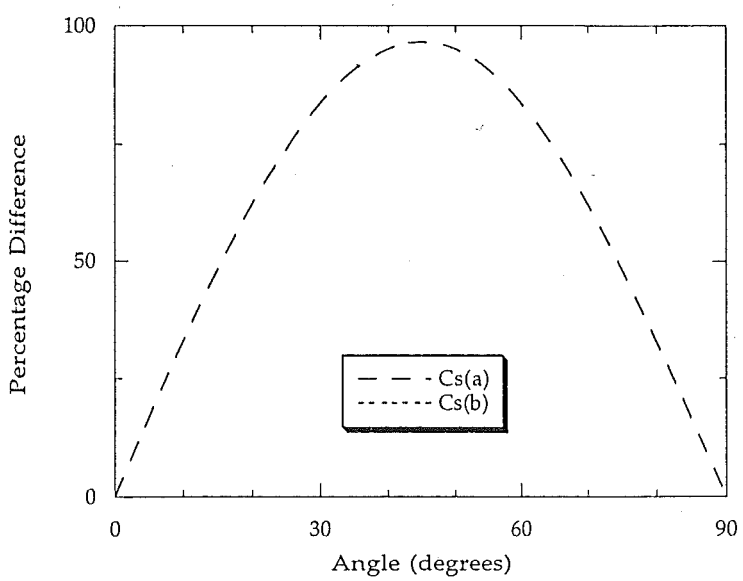

Figure 2.19: $\gamma_1(Z)\gamma_2$ transition interference predictions from the non-interfering equation (2.4) and the generalised interfering form (2.3) denoted by "+ i". Intensities for each site are summed over all centre orientations (tables 2.5, 2.6) with all amplitudes set to unity. There is no interference for the $C_s(b)$ centres.

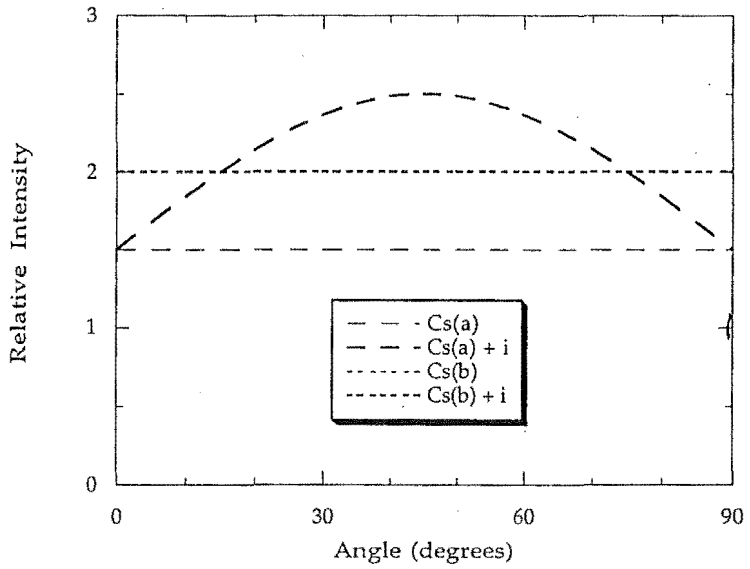

Figure 2.20: $\gamma_1(Z)\gamma_2$ relative interference. Difference between the interfering and non-interfering curves above (cross-term of equation (2.3)), as a percentage of the latter (equation (2.4)).

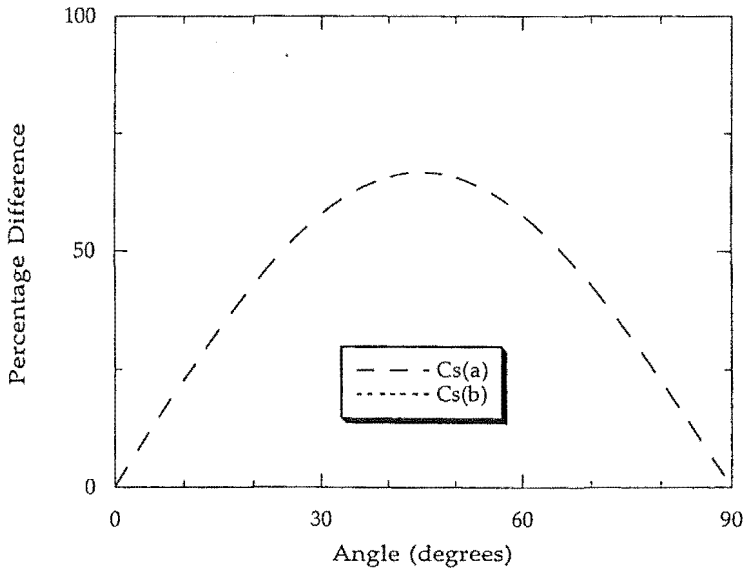

Figure 2.21: $\gamma_2(Y)\gamma_1$ transition interference predictions from the non-interfering equation (2.4) and the generalised interfering form (2.3) denoted by "+ i". Intensities for each site are summed over all centre orientations (tables 2.5, 2.6) with all amplitudes set to unity. There is no interference for the $C_s(b)$ centres.

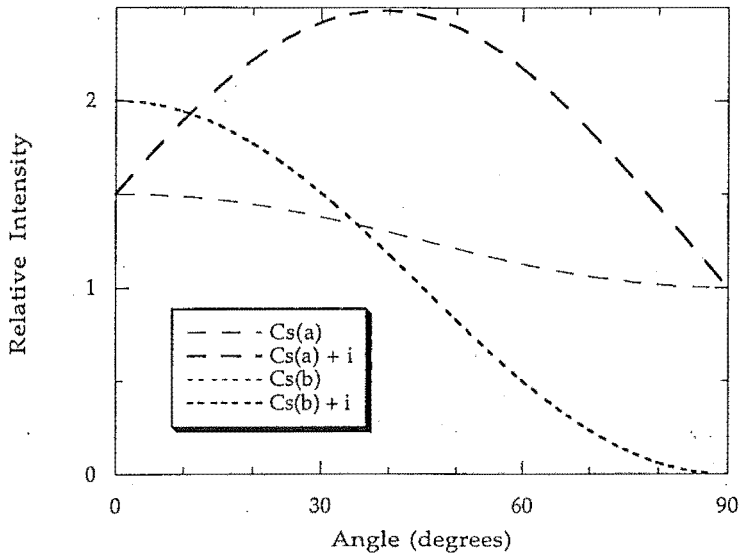

Figure 2.22: $\gamma_2(Y)\gamma_1$ relative interference. Difference between the interfering and non-interfering curves above (cross-term of equation (2.3)), as a percentage of the latter (equation (2.4)).

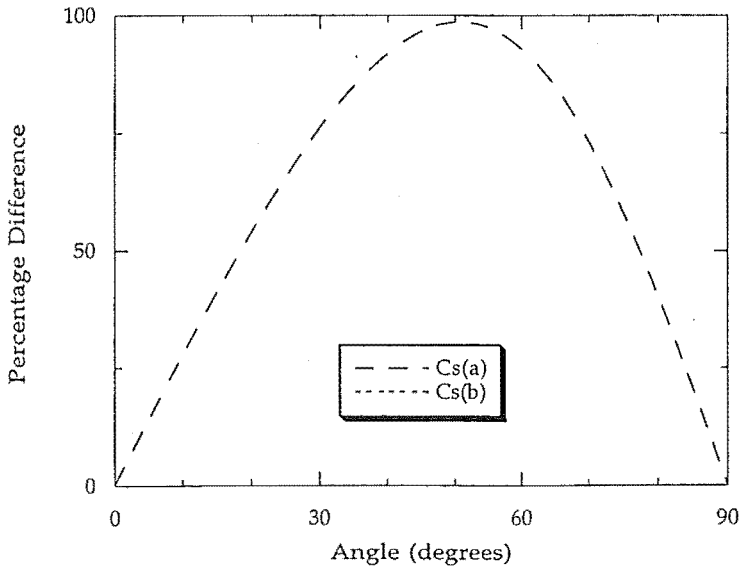

Figure 2.23: $\gamma_2(Y)\gamma_2$ transition interference predictions from the non-interfering equation (2.4) and the generalised interfering form (2.3) denoted by "+ i". Intensities for each site are summed over all centre orientations (tables 2.5, 2.6) with all amplitudes set to unity. There is no interference for the $C_s(b)$ centres.

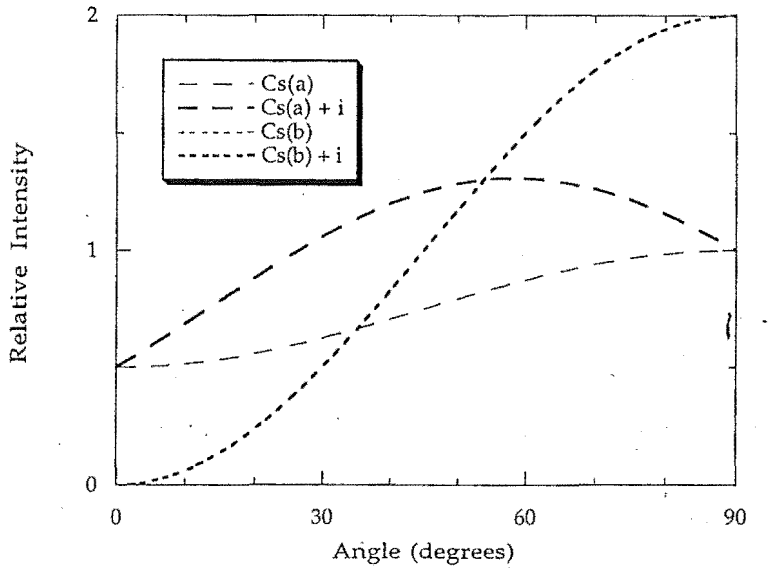

Figure 2.24: $\gamma_2(Y)\gamma_2$ relative interference. Difference between the interfering and non-interfering curves above (cross-term of equation (2.3)), as a percentage of the latter (equation (2.4)).

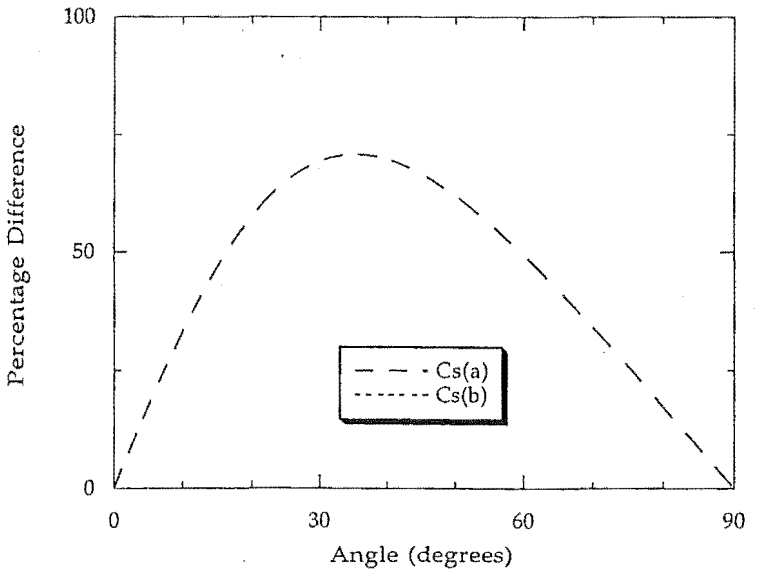

Figure 2.25: $\gamma_2(Z)\gamma_1$ transition interference predictions from the non-interfering equation (2.4) and the generalised interfering form (2.3) denoted by "+ i". Intensities for each site are summed over all centre orientations (tables 2.5, 2.6) with all amplitudes set to unity.

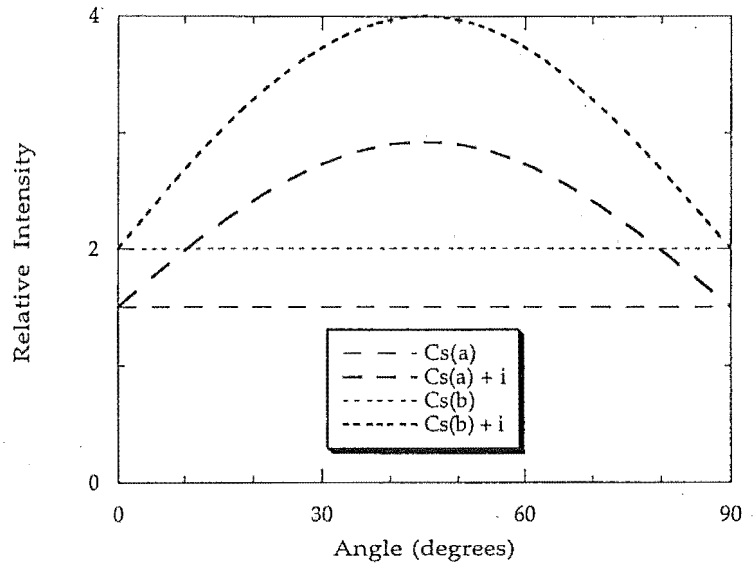

Figure 2.26: $\gamma_2(Z)\gamma_1$ relative interference. Difference between the interfering and non-interfering curves above (cross-term of equation (2.3)), as a percentage of the latter (equation (2.4)).

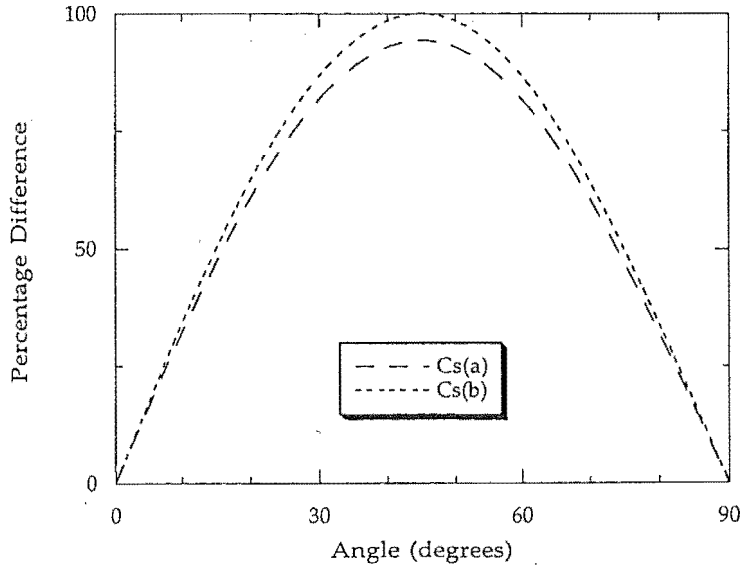

Figure 2.27: $\gamma_2(Z)\gamma_2$ transition interference predictions from the non-interfering equation (2.4) and the generalised interfering form (2.3) denoted by "+ i". Intensities for each site are summed over all centre orientations (tables 2.5, 2.6) with all amplitudes set to unity. There is no interference for either class of centres, and the $C_s(b)$ site has zero intensity to boot.

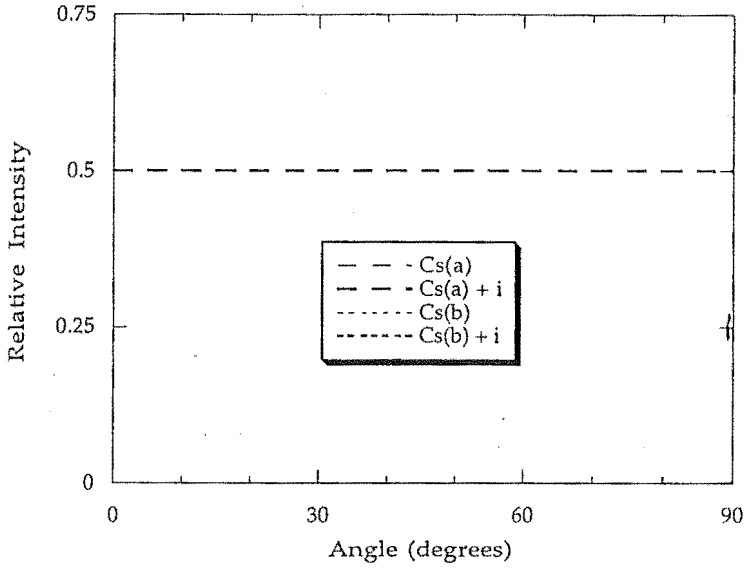

Figure 2.28: $\gamma_2(Z)\gamma_2$ relative interference. Difference between the interfering and non-interfering curves above (cross-term of equation (2.3)), as a percentage of the latter (equation (2.4)).

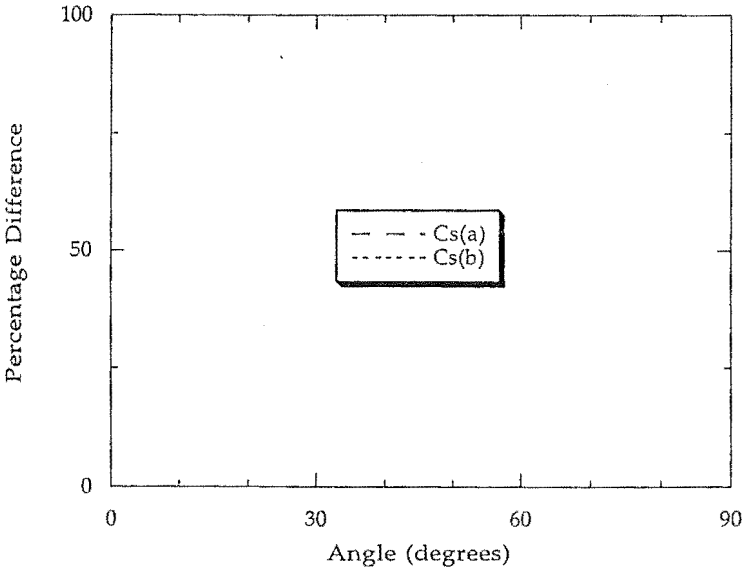

2.5 Practical Considerations

Concerns have been raised (see acknowledgements) that the expected crystal-relative interference effects may in practice be masked for these multi-hydrogenic rare-earth centres. Bulk hydrogenated CaF_2:Pr^{3+} crystals contain all the previously mentioned symmetry sites, C_{4v}, C_{2v}, C_s and C_1, at every possible orientation to the X, Y, Z axes. Techniques are available which can selectively excite only sites of a chosen symmetry [31], but it is not possible to excite only one orientation. For $C_s(a)$ sites the different centres are at rakish angles to both the crystal planes and each other (figure 2.9) making it impossible to simultaneously excite less than four distinct orientations. With $C_s(b)$ symmetry, all orientations have centre-relative axes which overlap (figure 2.10) and at best just two orientations having a common x-y plane may be excited.

However, the intensity predictions presented in figures 2.13 through 2.28 were calculated by summing over all possible orientations, with equal weighting, for both types of centres and the effects shown are large, up to 100% difference. All orientations tend to interfere in the same way $(d^*e + e^*d)$, under a given crystal relative polarised transition (tables 2.3, 2.4, 2.5, 2.6), and any deviation from equation (2.2) would be indicative of interference, the masking would have to be a 100% cancellation of interference to totally hide the difference and alter the conclusions.

As an alternative to using this multi-oriented centre hydrogenated CaF_2:Pr^{3+} system it would be possible to create C_s sites of only one orientation by applying a transverse electric field to some nominally uniaxial crystal. Such systems have been studied for transverse Zeeman effect phenomena, but a potential difficulty is that the uniaxial to C_s split transitions have intensities differing by as much as an order of magnitude. As noted, this would also make interference detection difficult.

2.6 Summary

Numerical calculations have suggested that low symmetry C_s sites should indeed display interference for fluorescence intensities of the centre relative x and y axes (*i.e* within the C_s plane), whilst higher symmetry sites (*e.g.* D_2, C_{4v}) should not. The predicted effect is large, being up to twice the intensity expected without interference. None of the experimental difficulties raised thus far appear to be insurmountable and for the most part are overcome by choice of a cubic structured host crystal.

With unity valued transition moment amplitudes, the most suitable interference transitions would be a $C_s(a)$ $\gamma_1(Z)\gamma_1$ transition, both centres in a $\gamma_2(Z)\gamma_1$ transition, or either centre with $\gamma_1(Y)\gamma_1$. Unfortunately the requisite data to identify specific transitions in hydrogenated CaF_2:Pr^{3+} is unavailable, but [27] lists the necessary information for deuterated SrF_2:Pr^{3+} which is isostructural to the former compound. None of the $C_s(b)$ transitions listed were useful, having polarisation ratios of 1:0 which produces no interference. Refering to figures 1.1 and 2.11, potential $C_s(a)$ transitions of interest include

- $^3H_4$ ground state (γ_1 irrep) to lowest $^1D_2$ level (γ_1) excitation, followed by immediate emission from this level to either of the two lowest $^3H_6$ levels (γ_1 or γ_2).

- $^3H_4$ ground state to $^3P_0$ (γ_1), then phononic loss to the lowest $^1D_2$ level from which fluorescence returns to the ground state.

All the transitions considered are for a Y polarised excitation beam and have polarisation ratios of 1:2. The first of these is either $\gamma_1(Y)\gamma_1$ or $\gamma_1(Y)\gamma_2$ depending upon which $^3H_6$ level is the final state, whilst the second possibility is $\gamma_1(Y)\gamma_1$ only. These could well be worth looking at experimentally, but it would still be preferable to identify and test some of the hydrogenated CaF_2:Pr^{3+} transitions noted above.

References

[1] P. W. Atkins. *Physical Chemistry.* Oxford University Press, Oxford, 4th edition, 1992.

[2] B. H. Brandow. *Effective Interactions and Operators in Nuclei*, volume 40, chapter 1 *Perturbation Theory of Effective Hamiltonians*, pages 1–24. Springer, Berlin, 1975. Edited by B. R. Barrett.

[3] A. R. Bryson and M. F. Reid. Transition amplitude calculations for one- and two-photon absorbtion. *J Alloys Comp*, 275-277:284–287, 1998.

[4] G. W. Burdick and F. S. Richardson. Correlation-crystal-field 'δ-function' analysis of $Pr^{3+}(4f^2)$ energy-level structure. *J Alloys Comp*, 250:293–296, 1997. Deals with a subset of the material in [5].

[5] G. W. Burdick and F. S. Richardson. Application of the correlation-crystal-field delta-function model in analyses of $Pr^{3+}(4f^2)$ energy-level structures in crystalline hosts. *Chem Phys*, 228(1-3):81–101, March 1998.

[6] W. T. Carnall, G. L. Goodman, K. Rajnak, and R. S. Rana. A systematic analysis of the spectra of the lanthanides doped into single crystal LaF_3. *J Chem Phys*, 90(7):3443–3457, April 1989.

[7] C. D. Churcher. *Polarisation Dependence of Multiphoton Spectroscopy.* PhD thesis, University of Canterbury, 1981.

[8] C. D. Churcher and G. E. Stedman. Symmetry restrictions for natural and induced circular dichroism and optical activity for all point groups. *J Phys C*, 15:5507–5520, 1982.

[9] H. M. Crosswhite and H. Crosswhite. Parametric model for f-shell configurations. I. The effective-operator Hamiltonian. *J Opt Soc Am B*, 1(2):246–254, April 1984.

[10] L. Esterowitz, F. J. Bartoli, R. E. Allen, D. E. Wortman, C. A. Morrison, and R. P. Leavitt. Energy levels and line intensities of Pr^{3+} in $LiYF_4$. *Phys Rev B*, 19(12):6442–6455, June 1979.

[11] M. D. Faucher and O. K. Moune. $4f^2/4f6p$ configuration interaction in $LiYF_4:Pr^{3+}$ *Phys Rev A*, 55(6):4150–4154, June 1997.

[12] M. D. Faucher and O. K. Moune. Notorious discrepancies in crystal field analyses eliminated by configuration interaction. *J Alloys Comp*, 250:306–309, 1997.

[13] S. Hüfner. *Optical Spectra of Transparent Rare Earth Compounds.* Academic Press, New York, 1978.

[14] V. Hurtubise and K. F. Freed. The Algebra of Effective Hamiltonians and Operators: Exact Operators. *Adv Chem Phys*, 83:465–541, 1993.

[15] V. Hurtubise and K. F. Freed. The algebra of effective Hamiltonians and operators: Truncated operators and computational aspects. *J Chem Phys*, 99(10):7946–7969, November 1993.

[16] V. Hurtubise and K. F. Freed. Perturbative and complete model space linked diagrammatic expansions for the canonical effective operator. *J Chem Phys*, 100(7):4955–4968, April 1994.

[17] C. K. Jayasankar and F. S. Richardson. Spin-Correlated Crystal-Field Analyses of the $4f^2(Pr^{3+})$ Energy Levels in $LiYF_4:Pr^{3+}$ and $LiBiF_4:Pr^{3+}$. *Phys Stat Sol B*, 155:221–230, 1989. An analysis of the results in [10].

[18] B. R. Judd. In P. Kramer and A. Riekers, editors, *Group Theoretical Methods in Physics*, volume 79 of *Lecture Notes in Physics*, page 417, Berlin, 1978. Springer-Verlag.

[19] B. R. Judd and H. Crosswhite. Orthogonalized operators for the f shell. *J Opt Soc Am B*, 1(2):255–260, April 1984.

[20] Y. L. Khong. *Solid State Spectroscopy: Laser Spectroscopy of Praseodymium doped Mixed Alkaline Earth Fluorides.* PhD thesis, University of Canterbury, 1991.

[21] Y. L. Khong, G. D. Jones, and R. W. G. Syme. Laser-selective-excitation spectroscopy of Pr^{3+} centers in mixed alkaline-earth-fluoride crystals. *Phys Rev B*, 48(2):672–686, July 1993.

[22] C. L. Li and M. F. Reid. Correlation-crystal-field analysis of the $^2H(2)_{11/2}$ multiplet of Nd^3+. *Phys Rev B*, 42(4):1903–1909, August 1990.

[23] I. Lindgren and J. Morrison. *Atomic many-body theory.* Number 3 in Springer series on Atoms and Plasmas. Springer-Verlag, New York, 2nd edition, 1986.

[24] M. Malinowski, M. F. Joubert, and B. Jacquier. Dynamics of the IR-to-blue wavelength upconversion in Pr^{3+}-doped yttriumm aluminium garnet and $LiYF_4$ crystals. *Phys Rev B*, 50(17):12367–12374, November 1994.

[25] C. H. Martin and K. F. Freed. *Ab Initio* Computation of Semiempirical π-Electron Methods. 4. True and Approximate Effective Hamiltonians for Hexatriene and Related Conjugated Polyenes. *J Phys Chem*, 99(9):2701–2716, February 1995.

[26] D. P. McLeod. Intensity Patterns of Hyperfine Split Energy Levels in Rare Earth Compounds. Master's thesis, University of Canterbury, 1996.

[27] K. M. Murdoch. *Laser Spectroscopy, Energy-Transfer and Bleaching Processes in Crystalline Rare-Earth Centres.* PhD thesis, University of Canterbury, 1993. The more pertinent material also appears in [28].

[28] K. M. Murdoch and G. D. Jones. Site symmetries, bleaching behaviour, and thermal stability of hydrogenic centers in $SrF_2:Pr^{3+}$ and $CaF_2:Pr^{3+}$. *Phys Rev B*, 58(18):12020–12037, November 1998. Expands on sections of [27].

[29] K. F. Purcell and J. C. Kotz. *Inorganic Chemistry.* Holt-Saunders, Hong Kong, 1977.

[30] J. R. Quagliano, G. W. Burdick, D. P. Glover-Fischer, and F. S. Richardson. Electronic absorbtion spectra, optical line strengths, and crystal field energy-level structure of Nd^{3+} in hexagonal $[Nd(H_2O)_9](CF_3SO_3)_3$. *Chem Phys*, 201(2,3):321–342, 1995.

[31] R. J. Reeves. *Laser Selective Excitation of Praseodymium ions in Hydrogenated Fluorite Crystals.* PhD thesis, University of Canterbury, 1987.

[32] M. F. Reid. Correlation crystal field analyses with orthogonal operators. *J Chem Phys*, 87(5):2875–2884, September 1987.

[33] M. F. Reid. Recent extensions to crystal-field and transition-intensity models. *J Alloys Comp*, 180:93–103, 1992.

[34] M. F. Reid. *The Crystal-Field Handbook*, chapter 14 *Transition Intensities*. Cambridge University Press, 1998. Edited by D. Newman and B. Ng.

[35] E. Schultheiss, A. Scharmann, and D. Schwabe. Energy Levels of Triply Ionized Praseodymium in $BiLiF_4$ Crystals. *Phys Stat Sol B*, 140:173–189, 1987.

[36] G. E. Stedman. A diagram technique for coupling calculations in compact groups. *J Phys A*, 8(7):1021–1037, 1975.

[37] G. E. Stedman. A diagram technique for basis functions and their transformation, with application to group-subgroup bases and crystal tensors. *J Phys A*, 9(12):1999–2019, 1976.

[38] G. E. Stedman. Polarization dependence of natural and field-induced one-photon and multiphoton interactions. *Adv Phys*, 34(4):513–587, 1985. Makes use of the diagram notation in [39].

[39] G. E. Stedman. *Diagram techniques in group theory.* Cambridge University Press, Cambridge, 1990. See also the earlier papers [36, 37].

[40] J. E. Stevens, R. K. Chaudhuri, and K. F. Freed. Global three-dimensional potential energy surfaces of H_2S from the *ab initio* effective valence shell Hamiltonian method. *J Chem Phys*, 105(19):8754–8768, November 1996.

[41] Q. Wang. *Selection Rules for Effective Intra-Atomic and Optical Transition Operators in Lanthanide Ions.* PhD thesis, University of Canterbury, 1993.

Moof!